

manuscript submitted to *JGR: Oceans*

**1      Can mesoscale eddy kinetic energy sources and sinks be  
2      inferred from sea surface height in the Agulhas Current  
3      ?**

**4      P. Tedesco<sup>1,2</sup>, J. Gula<sup>1,3</sup>, P. Penven<sup>1</sup>, C. Ménesguen<sup>1</sup>, Q. Jamet<sup>4</sup>, C. Vic<sup>1</sup>**

**5**      <sup>1</sup>Univ. Brest, CNRS, IRD, Ifremer, Laboratoire d'Océanographie Physique et Spatiale (LOPS), IUEM,  
**6**      29280, Brest, France.

**7**      <sup>2</sup>Imperial College of London, London, UK.

**8**      <sup>3</sup>Institut Universitaire de France (IUF), Paris, France.

**9**      <sup>4</sup>Institut des Géosciences de l'Environnement (IGE), Grenoble, France.

**10     Key Points:**

- 11** The mesoscale *EKE* flux divergence is overall positive in the Agulhas Current region,  
12     highlighting a net mesoscale *EKE* source
- 13** Coupled geostrophic-ageostrophic *EKE* flux significantly contributing to the net  
14     *EKE* source cannot be inferred using sea surface height
- 15** Advection done by geostrophic *EKE* flux dominates the net *EKE* source and can  
16     be inferred using sea surface height

---

Corresponding author: Pauline Tedesco, p.tedesco@imperial.ac.uk

17 **Abstract**

18 Western boundaries (WB) have been suggested to be hotspots of mesoscale eddy decay,  
 19 using an eddy kinetic energy (*EKE*) flux divergence based on sea surface height ( $\eta$ ). The  
 20  $\eta$ -based diagnostic requires approximations, including the use of geostrophic velocities. Here,  
 21 we assess to what extent mesoscale *EKE* flux divergence can be inferred from  $\eta$  using a  
 22 numerical simulation of the Agulhas Current. The *EKE* flux divergence is composed of two  
 23 terms: the eddy-pressure work (linear component) and the advection of *EKE* (nonlinear  
 24 component). Both are mainly positive in the WB region (net *EKE* sources). However,  
 25 it is not reliably accounted by  $\eta$ -based diagnostics. The  $\eta$ -based eddy-pressure work has a  
 26 net contribution in the WB region of the opposite sign than the true one. Ageostrophic  
 27 eddy-pressure work dominates the geostrophic one (corresponding to a  $\beta$ -contribution). It  
 28 is explained by mesoscale eddies's scale to fall below the scale of  $\frac{\zeta'_{RMS}}{\beta}$  ( $\zeta'_{RMS}$ : normalized  
 29 relative vorticity for mesoscale eddies;  $\beta$ : latitudinal variations of Coriolis parameter). The  
 30 advection of *EKE* done by geostrophic *EKE* flux dominates the *EKE* flux divergence in the  
 31 WB region. It results in the *EKE* flux divergence to be qualitatively estimable using  $\eta$  (up  
 32 to 54% of the net *EKE* source). Our results in the Agulhas Current show a mesoscale eddy  
 33 dynamics in contrast with the decay's paradigm at western boundaries. Further analysis in  
 34 other western boundaries are required to complete our understanding of mesoscale eddies  
 35 dynamics.

36 **Plain Language Summary**

37 Large-scale eddies are a key component of the ocean energy budget. Although their  
 38 generation is largely documented, how their energy is dissipated remains uncertain. A closure  
 39 to their lifecycle — decay at western boundaries of oceanic basins — has been suggested  
 40 using satellite observations of the sea surface. However, using sea surface observations re-  
 41 quires several approximations on the ocean dynamics. Understanding to what extent, the  
 42 large-scale eddies dynamics can be inferred from sea surface observations is a fundamen-  
 43 tal issue for study strategies. Here, we investigate the impacts of the approximations, on  
 44 the net energy sources and sinks of large-scale eddies, using a numerical simulation of the  
 45 Agulhas Current. We show that the Agulhas Current is a net energy source of large-scale  
 46 eddies, which can be qualitatively inferred using sea surface observations. The net energy  
 47 source is mainly explained by turbulent motions and more weakly, but still significantly by  
 48 wave-like motions. The leading order velocities of turbulent motions can be inferred from  
 49 sea surface observations. Our results in the Agulhas Current are favorable to the use of sea  
 50 surface observations, but show a dynamics in contrast with the decay's paradigm at western  
 51 boundaries.

52 **1 Introduction**

53 Mesoscale eddies represent 90 % of the surface kinetic energy (Wunsch, 2007) and are  
 54 a key component of the global ocean energy budget (Ferrari & Wunsch, 2009; Müller et  
 55 al., 2005). They have horizontal scales of the order of the 1<sup>st</sup> Rossby deformation radius  
 56 ( $Rd$ ) or larger (Chelton et al., 2011). At these scales, the velocity field can be decomposed  
 57 into a leading order geostrophic and a weaker ageostrophic component based on the quasi-  
 58 geostrophic theory (Gill, 1982). Geostrophy represents the balance of flows dominated by  
 59 rotation compared to advection (Rossby number :  $Ro \ll 1$ ) and stratification compared to  
 60 vertical shear (Richardson number :  $Ri \gg 1$ ). At scales comparable to or smaller than  $Rd$ ,  
 61 the dynamics departs from geostrophy ( $Ro, Ri \sim O(1)$ ) and ageostrophic effects, such as  
 62 advection, vertical shear and topographic interactions among others, can play an important  
 63 role.

64

65 The characteristics of mesoscale eddies make them easily trackable by satellite altimetry,  
 66 which measures sea surface height ( $\eta$ ). The low-frequency component of sea-surface height  
 67 is an indirect measure of the surface geostrophic currents. Satellite altimetry allowed to im-  
 68 prove our understanding of the ocean dynamics by evidencing the prevalence of mesoscale  
 69 eddies at the surface (Ducet et al., 2000). Although mesoscale eddies are ubiquitous across  
 70 the ocean, they are the most energetic in western boundary currents and in the Antarctic  
 71 Circumpolar Current (Ducet et al., 2000; Chelton et al., 2007, 2011), making these regions  
 72 key spots for the global ocean energy budget.  
 73

74 Western boundaries have been suggested to be mesoscale eddy kinetic energy (*EKE*)  
 75 sinks (Zhai et al., 2010). This suggestion closes the following paradigm of mesoscale eddy  
 76 lifecycle: mesoscale eddies originate nearly everywhere in the ocean, propagate westward  
 77 at about the speed of long baroclinic Rossby waves and decay upon western boundaries,  
 78 likely due to direct energy routes, down to dissipation, channeled by topography (Gill et  
 79 al., 1974; Zhai et al., 2010; Chelton et al., 2011; Evans et al., 2020; Z. Yang et al., 2021;  
 80 Evans et al., 2022). This scenario has been confirmed, using *in situ* measurements and  
 81 idealized numerical simulations, in regions free of western boundary current (Evans et al.,  
 82 2020; Z. Yang et al., 2021; Evans et al., 2022). However, in the presence of western boundary  
 83 currents, studies based on numerical simulations show more complex mesoscale eddy dy-  
 84 namics. Western boundaries are hotspots of mesoscale eddy generation due to instabilities  
 85 of the western boundary currents (Halo et al., 2014; Kang & Curchitser, 2015; Gula et al.,  
 86 2015; Y. Yang & Liang, 2016; Yan et al., 2019; Li et al., 2021; Jamet et al., 2021; Tedesco  
 87 et al., 2022), such that local generation of mesoscale eddies may overcome the local decay  
 88 of remotely-generated mesoscale eddies.  
 89

90 Sources and sinks of mesoscale *EKE* can be estimated by computing the *EKE* flux  
 91 divergence. A negative (positive) *EKE* flux divergence shows a net *EKE* sink (source).  
 92 The *EKE* flux divergence corresponds to the rate of the spatial redistribution of *EKE*. It  
 93 has two components : the work done by pressure fluctuations (eddy-pressure work; usually  
 94 interpreted as the linear contribution from the waves) and the nonlinear advection of *EKE*  
 95 by the flow (Harrison & Robinson, 1978).  
 96

97 Using an  $\eta$ -based *EKE* flux divergence, Zhai et al. (2010) estimated a mesoscale *EKE*  
 98 sink. Their vertically-integrated *EKE* flux divergence based on  $\eta$  relies on three approxi-  
 99 mations:

- 100    (i) **Mesoscale eddies are assumed to be geostrophic.** Geostrophy should be a good  
 101       approximation for mesoscale eddy velocities, as assumed by the quasi-geostrophic  
 102       turbulence theory (Charney, 1971) and indicated by the Rossby number of mesoscale  
 103       eddies ( $Ro = O(\ll 0.05)$ ) inferred from satellite altimetry (Chelton et al., 2011).
- 104    (ii) **The mesoscale eddy vertical structure is approximated by the 1<sup>st</sup> baro-  
 105       clinic mode.**  $\eta$  is a measure of the ocean surface dynamics and is usually interpreted  
 106       as primarily reflecting the 1<sup>st</sup> baroclinic mode, which has a surface-intensified struc-  
 107       ture (Wunsch, 1997; Smith & Vallis, 2001). It relates to mesoscale eddies which  
 108       have surface-intensified vertical structures energized to the bottom, represented by  
 109       the combination of the barotropic and 1<sup>st</sup> baroclinic vertical modes (Wunsch, 1997;  
 110       Smith & Vallis, 2001; Venaille et al., 2011; Tedesco et al., 2022).
- 112    (iii) **Mesoscale eddies interactions with topography are neglected.** This might  
 113       be justified by assuming that mesoscale *EKE* flux have spatial variations larger than  
 114       that of topography (Zhai et al., 2010).

Several studies, based on numerical simulations and using no approximations, denote a *EKE* flux divergence in contrast with the  $\eta$ -based one (Harrison & Robinson, 1978; Chen et al., 2014; Capó et al., 2019). The eddy-pressure work is mainly negative and of leading order in most regions (western boundary currents, Antarctic Circumpolar Current, Subtropical gyre and Interior Ocean). The advection of *EKE* is positive in most western boundary currents and in the Western Mediterranean Sea, but it is the leading order contribution only in the latter region. It indicates that the eddy-pressure work and advection of *EKE* have contrasted contributions, resulting in an *EKE* flux divergence varying between western boundaries. A recent study has shown that both mesoscale eddy-pressure work and advection of *EKE* are positive in the Agulhas Current region (Tedesco et al., 2022). This region is a net mesoscale *EKE* source, in contrast with the paradigm of net mesoscale *EKE* sinks at western boundaries.

128

The differences between the non-approximated and the  $\eta$ -based *EKE* flux divergence question the approximations used to derive the  $\eta$ -based diagnostic. Due to the leading order geostrophic component of mesoscale eddy, satellite altimetry is a reference database for evaluating the surface mesoscale *EKE* reservoir. However, the question of using altimetry data to assess the sources and sinks of mesoscale *EKE* remains a separate issue. The quasi-geostrophic theory states that ageostrophic motions significantly contribute to the processes sustaining the mesoscale *EKE* reservoir (Müller et al., 2005; Ferrari & Wunsch, 2009). While the significance of ageostrophic motions to energy transfers across scales, and especially from mesoscale eddies toward smaller scales, is asserted, its contributions to the *EKE* flux divergence remains an open question to our knowledge.

139

Surface geostrophic velocities derived from satellite altimetry data are usually interpreted as primarily reflecting the 1<sup>st</sup> baroclinic mode (Wunsch, 2007; Smith & Vallis, 2001). However, this questions the interpretation of the  $\eta$ -based *EKE* flux divergence as the one of the mesoscale reservoir, which is formally represented by the barotropic and 1<sup>st</sup> baroclinic modes (Wunsch, 1997; Smith & Vallis, 2001; Venaille et al., 2011). This question is supported by a study showing that the increasing resolution of eddies results in an increasing *EKE* fraction into the baroclinic mode (Yankovsky et al., 2022). It is also supported by a study showing that the mesoscale *EKE* reservoir is equipartitioned between both modes, or even locally dominated by the barotropic mode, in the western boundary region of the Agulhas Current (Tedesco et al., 2022).

150

Topographic interactions are documented to be key processes of mesoscale eddy dynamics at western boundaries. Topography controls instability processes (Lutjeharms, 2006; Gula et al., 2015) and channels energy transfers between mesoscale eddies, eddies of smaller scale, waves and mean currents (Adcock & Marshall, 2000; Nikurashin & Ferrari, 2010; Evans et al., 2020; Perfect et al., 2020; Tedesco et al., 2022). The contribution of topographic interactions to mesoscale *EKE* flux divergence remains to be determined.

157

Assessing to what extent altimetry data allows to infer mesoscale *EKE* flux divergence is an important step toward improving our understanding of the global ocean dynamics. It depends on the impact of the three aforementioned approximations – (i) geostrophy *vs.* ageostrophy, (ii) 1<sup>st</sup> baroclinic *vs.* barotropic modes and (iii) importance of topographic interactions – in regions of western boundary. We aim to assess the impact of approximations (i), (ii), and (iii) on the mesoscale *EKE* flux divergence using a numerical simulation of the Agulhas Current. The latter one is the western boundary current of the South Indian Ocean (Lutjeharms, 2006) and a sub-region of the largest mesoscale *EKE* sink, found at the western boundary of the South Indian Ocean, by Zhai et al. (2010).

166

Our study is organized around the following questions : Do the  $\eta$ -based components of the *EKE* flux divergence (eddy-pressure work and advection of *EKE*) provide reliable estimates of the true ones ? If not, which approximations are responsible for differences ? What are the implications for inferring the *EKE* flux divergence using  $\eta$  field ? The true and  $\eta$ -based expressions of *EKE* flux divergence components (eddy-pressure work and advection of *EKE*) are defined and interpreted in section 2. The  $\eta$ -based paradigm of mesoscale *EKE* sink at western boundaries (Zhai et al., 2010) is evaluated using observations and a numerical simulation in section 3. The validity of the  $\eta$ -based components are evaluated and the main contributions of the true components are characterized, respectively in section 4 and 5. The results of sections 4 and 5 are sum up in section 6 to draw a conclusion on the use of satellite altimetry data to infer the *EKE* flux divergence. The results are then discussed in a larger context of observation-based *EKE* budgets and of mesoscale eddy dynamics in section 7.

## 2 Theory

We present in the following the modal *EKE* flux divergence. We first present the theoretical framework of vertical modes. We then define the true expression of the *EKE* flux divergence, constituted of the modal eddy-pressure work (*EPW*) and the advection of *EKE* (*AEKE*), based on Tedesco et al. (2022). We finally detail the approximations that are required to derive their  $\eta$ -based expressions.

### 2.1 Vertical modes

A convenient approach to describe the vertical structure of mesoscale motions is the modal decomposition using traditional vertical modes (Gill, 1982). The vertical structure of the mesoscale *EKE* reservoir corresponds to the combination of the barotropic and 1<sup>st</sup> baroclinic modes (Wunsch, 1997; Smith & Vallis, 2001; Venaille et al., 2011; Tedesco et al., 2022), which represents surface-intensified vertical structures energized to the bottom.

The vertical modes  $\phi_n$  for the horizontal velocity ( $\mathbf{u}$ ) and the dynamical pressure ( $p$ ) are the eigenfunctions solution of the Sturm-Liouville problem (Eq. 1), using linearized free-surface ( $| \frac{\partial}{\partial z} \phi_n |_{z=\eta} = | \frac{-N^2}{g} \phi_n |_{z=\eta} \rangle$ ) and flat-bottom boundary conditions ( $| \frac{\partial}{\partial z} \phi_n |_{z=-H} = 0 \rangle$  :

$$\frac{\partial}{\partial z} \left( \frac{1}{N^2} \frac{\partial}{\partial z} \phi_n \right) + \frac{1}{c_n^2} \phi_n = 0 \quad (1)$$

with  $N^2$  the time-averaged buoyancy frequency,  $g$  the acceleration of gravity and  $c_n^2 = \frac{1}{n\pi} \int_{-H}^{\eta} N(\mathbf{x}, z) dz$  the eigenvalues of the vertical modes.

The vertical modes are related to horizontal scales via  $c_n^2$ , which are good approximations of the Rossby baroclinic deformation radii :  $Rd_{n \geq 1} = \frac{c_n}{|f|}$  (Chelton et al., 1998), with  $f$  the Coriolis parameter. The modal base  $\phi_n$  satisfies the orthogonality condition :

$$\int_{-H}^{\eta} \phi_m \phi_n dz = \delta_{mn} h \quad (2)$$

with  $\delta_{mn}$  the usual Kronecker symbol and  $h = \eta + H$  the water column depth.

The dynamical variables are projected onto  $n$  vertical modes as follows :

$$[\mathbf{u}_n(\mathbf{x}, t), \frac{1}{\rho_0} p_n(\mathbf{x}, t)] = \frac{1}{h} \int_{-H}^{\eta} [\mathbf{u}(\mathbf{x}, z, t), \frac{1}{\rho_0} p(\mathbf{x}, z, t)] \phi_n(\mathbf{x}, z) dz \quad (3)$$

with  $\mathbf{u}_n$  and  $p_n$  the modal amplitudes of the horizontal velocity ( $\mathbf{u}$ ) and dynamical pressure ( $p$ ) and  $\rho_0$  the reference density value.

## 2.2 True expression of the modal *EKE* flux divergence

The modal *EKE* flux divergence is a contribution of the modal *EKE* budget. The modal *EKE* budget corresponds to the classic *EKE* budget (Harrison & Robinson, 1978; Gula et al., 2016) derived in the framework of the vertical modes. Tedesco et al. (2022) derived a comprehensive modal *EKE* budget in the context of the mesoscale variability, inspired from the budget derived in the context of internal tides (Kelly, 2016). The modal *EKE* budget reads as follows :

$$\begin{aligned}
& \underbrace{\mathbf{u}'_{\mathbf{n}} \cdot \left( \rho_0 h \frac{\partial}{\partial t} \mathbf{u}'_{\mathbf{n}} \right)}_{\text{Time rate}} + \underbrace{\nabla_H \cdot \int_{-H}^H \mathbf{u}'_{\mathbf{n}} p'_n \phi_n^2 dz}_{\text{Eddy-pressure work (EPW)}} + \underbrace{\frac{\rho_0}{2} \nabla_H \cdot \int_{-H}^H \mathbf{u}_{\mathbf{n}} \phi_n \|\mathbf{u}'_{\mathbf{n}} \phi_n\|^2 dz}_{\text{Advection of EKE (AEKE)}} \\
& \qquad \qquad \qquad \underbrace{\text{Modal EKE flux divergence (EPW+AEKE)}} \\
& = \sum \left( \underbrace{S_n}_{\text{EKE sources}} + \underbrace{D_n}_{\text{EKE sinks}} \right) \tag{4}
\end{aligned}$$

with the prime denoting fluctuations relative to the 1995-2004 time average. Terms are averaged over this period. The dynamical pressure ( $p(\mathbf{x}, z, t)$ ) is derived from the *in situ* density ( $\rho(\mathbf{x}, z, t)$ ) from which the background density profile ( $\tilde{\rho}(z)$  defined as the spatial and time average of the *in situ* density) has been subtracted.

The modal  $EKE$  flux divergence corresponds to the rate of the spatial redistribution of modal  $EKE$  done by pressure fluctuations ( $EPW$ ) and by advection ( $AEKE$ ). The  $EPW$  is usually interpreted as the linear wave contribution, and  $AEKE$  as the advection of  $EKE$  by the total flow (Harrison & Robinson, 1978). In the context of linear theories of internal waves (Kelly et al., 2010, 2012; Kelly, 2016) and of Rossby waves (Masuda, 1978),  $EPW$  is the only contribution to the modal  $EKE$  flux divergence. For interior-ocean dynamics it represents the main contribution (Harrison & Robinson, 1978). In regions of high variability,  $AEKE$  can significantly contribute to the  $EKE$  flux divergence and can be equivalent to  $EPW$  (Harrison & Robinson, 1978; Capó et al., 2019; Tedesco et al., 2022).

The mesoscale eddy dynamics modeled by our numerical simulation is in equilibrium for the period considered in our study (1995-2004). The time rate smallness has indeed been evaluated by Tedesco et al. (2022) for the period 1995-1999, which is shorter than the period 1995-2004 used here. The modal *EKE* flux divergence therefore accounts for the left hand side of the modal *EKE* budget (Eq. 4). It equals the sum of all local *EKE* sources ( $S_n$ ) and sinks ( $D_n$ ). It can therefore be interpreted as the redistribution rate of the net *EKE* sources and sinks. A negative (positive) *EKE* flux divergence indicates that the ingoing *EKE* flux are larger (lower) than the outgoing ones, resulting in a net *EKE* sink (source), whose content has been imported (exported).

In the present study, we focus on the *EKE* flux divergence of the mesoscale reservoir, that we define as the sum of the barotropic ( $n = 0$ ) and  $1^{st}$  baroclinic ( $n = 1$ ) components ( $EPW_{n=0-1}$  and  $AEKE_{n=0-1}$  that are referred to *EPW* and *AEKE* in the following in order to simplify the notations)

### 2.3 $n$ -based expressions of the modal EKE flux divergence

We define the different  $\eta$ -based expressions of *EPW*, gradually accounting for approximations (i), (ii) and (iii) used in Zhai et al. (2010). We also define an  $\eta$ -based expression of *AEKE* accounting for approximation (i). The main terms discussed in this study are listed in Table 1.

237      **2.3.1 Approximation (i) ( $EPW_{(i)}$  and  $AEKE_{(i)}$ )**

238       $EPW$  and  $AEKE$  (Eq. 4) can be written as the sum of three contributions, as follows

239      :

$$EPW = \underbrace{\int_{-H}^{\eta} p'_n \phi_n \nabla_H \cdot (\mathbf{u}'_n \phi_n) dz}_{\mathbf{A}} + \underbrace{\int_{-H}^{\eta} (\mathbf{u}'_n \phi_n) \cdot \nabla_H (p'_n \phi_n) dz}_{\mathbf{B}} \\ + \underbrace{\nabla_H \eta \cdot |\mathbf{u}'_n p'_n \phi_n|^2|_{z=\eta} + \nabla_H H \cdot |\mathbf{u}'_n p'_n \phi_n|^2|_{z=-H}}_{\mathbf{C}} \quad (5)$$

$$AEKE = \underbrace{\frac{\rho_0}{2} \int_{-H}^{\eta} \|\mathbf{u}'_n \phi_n\|^2 \nabla_H \cdot (\mathbf{u}_n \phi_n) dz}_{\mathbf{A}} + \underbrace{\frac{\rho_0}{2} \int_{-H}^{\eta} (\mathbf{u}_n \phi_n) \cdot \nabla_H \|\mathbf{u}'_n \phi_n\|^2 dz}_{\mathbf{B}} \\ + \underbrace{\frac{\rho_0}{2} \nabla_H \eta \cdot |\mathbf{u}_n \phi_n| |\mathbf{u}'_n \phi_n|^2|_{z=\eta} + \frac{\rho_0}{2} \nabla_H H \cdot |\mathbf{u}_n \phi_n| |\mathbf{u}'_n \phi_n|^2|_{z=-H}}_{\mathbf{C}} \quad (6)$$

240      Terms **C** represent the interactions of  $EKE$  flux with topography ( $-H$ ) and sea surface  
 241      height ( $\eta$ ) gradients. It can be further simplified to interactions with topographic gradients,  
 242      because :  $\|\nabla_H \eta\| = O(10^{-4}) \|\nabla_H H\|$  in the Agulhas Current region.

243

244       $EPW$  (Eq. 5) and  $AEKE$  (Eq. 6) can be written as  $EPW_{(i)}$  (Eq. 7) and  $AEKE_{(i)}$  (Eq.  
 245      8) when using the approximation of (i) modal geostrophic velocities ( $\mathbf{u}'_{g,n} \phi_n$ ). The velocities  
 246      are expressed using modulated  $\eta$  fields, which account for the fraction of the different vertical  
 247      modes ( $\mathbf{u}_{g,n} \phi_n = \mathbf{k} \wedge \frac{g}{f} \nabla_H \left( \frac{\phi_n}{|\phi_n|_{z=0}} \lambda_n \eta \right)$  with  $\lambda_n = \frac{\eta_n}{\eta}$  and  $\mathbf{u}'_{g,n} \phi_n = \mathbf{k} \wedge \frac{g}{f} \nabla_H \left( \frac{\phi_n}{|\phi_n|_{z=0}} \alpha_n \eta' \right)$   
 248      with  $\alpha_n = \frac{\eta'_n}{\eta'}$ ).

$$EPW_{(i)} = - \underbrace{\frac{\beta \rho_0 g^2}{2f^2} \frac{\partial}{\partial x} \left( \underbrace{\int_{-H}^{\eta} \frac{\phi_n^2 dz}{|\phi_n^2|_{z=0}}}_{\beta\text{-contribution } (\mathbf{A1})} \alpha_n^2 \eta'^2 \right)}_{\beta\text{-contribution to topographic interactions } (\mathbf{A2})} + \underbrace{\frac{\beta \rho_0 g^2}{2f^2} \frac{\partial H}{\partial x} \frac{|\phi_n^2|_{z=-H}}{|\phi_n^2|_{z=0}} \alpha_n^2 \eta'^2}_{\beta\text{-contribution to topographic interactions } (\mathbf{A2})} \\ + \underbrace{\frac{\rho_0 g^2}{2f} \nabla_H H \cdot \mathbf{k} \wedge \nabla_H \left( \frac{\phi_n^2}{|\phi_n^2|_{z=0}} \right) \alpha_n^2 \eta'^2|_{z=-H}}_{EKE \text{ flux-topographic interactions } (\mathbf{C})} \quad (7)$$

With approximation (i), the contribution of horizontal modal pressure gradients (**B** in Eq. 5) cancels out.  $EPW_{(i)}$  is therefore constituted of a  $\beta$ -contribution acting on  $EKE$  flux (**A1**) and topographic interactions (**A2**) and of the contribution of  $EKE$  flux-topographic interactions (**C**).

$$AEKE_{(i)} = - \underbrace{\frac{\beta \rho_0 g}{2f^2} \int_{-H}^{\eta} \|\mathbf{u}'_{g,n} \phi_n\|^2 \frac{\partial}{\partial x} \left( \frac{\phi_n}{|\phi_n|_{z=0}} \lambda_n \eta \right) dz}_{\beta\text{-contribution } (\mathbf{A})} + \underbrace{\frac{\rho_0}{2} \int_{-H}^{\eta} (\mathbf{u}_{g,n} \phi_n) \cdot \nabla_H \|\mathbf{u}'_{g,n} \phi_n\|^2 dz}_{Work \text{ of eddy-total flow interactions } (\mathbf{B})} \\ + \underbrace{\frac{\rho_0}{2} \nabla_H H \cdot |\mathbf{u}_{g,n} \phi_n| |\mathbf{u}'_{g,n} \phi_n|^2|_{z=-H}}_{EKE \text{ flux-topographic interactions } (\mathbf{C})} \quad (8)$$

249  $AEKE_{(i)}$  (Eq. 8) is constituted of a  $\beta$ -contribution (**A**), the work of eddy-total flow inter-  
 250 actions (**B**) and of the  $EKE$  flux-topographic interactions (**C**).  
 251

### 252 2.3.2 Approximation (ii) ( $EPW_{(i,ii)}$ )

253  $EPW_{(i)}$  (Eq. 7) can be written as  $EPW_{(i,ii)}$  (Eq. 9) when using the approximation of  
 254 (ii)  $\eta$  primarily reflecting the 1<sup>st</sup> baroclinic mode ( $\alpha_n \sim \alpha_1 \sim 1$ ), such as :

$$255 EPW_{(i,ii)} = \underbrace{-\frac{\beta\rho_0g^2}{2f^2} \frac{\partial}{\partial x} \left( \frac{\int_{-H}^{\eta} \phi_1^2 dz}{|\phi_1^2|_{z=0}} \eta'^2 \right)}_{\beta\text{-contribution (A1)}} + \underbrace{\frac{\beta\rho_0g^2}{2f^2} \frac{\partial H}{\partial x} \frac{|\phi_1^2|_{z=-H}}{|\phi_1^2|_{z=0}} \eta'^2}_{\beta\text{-contribution to topographic interactions (A2)}} \\ (9) \\ + \underbrace{\frac{\rho_0g^2}{2f} \nabla_H H \cdot |\mathbf{k} \wedge \nabla_H \left( \frac{\phi_1^2}{|\phi_1^2|_{z=0}} \right) \eta'^2|_{z=-H}}_{EKE \text{ flux-topographic interactions (C)}}$$

### 256 2.3.3 Approximation (iii) ( $EPW_{(i,ii,iii)}$ and $EPW_{(i,iii)}$ )

257  $EPW_{(i,ii)}$  (Eq. 9) can be written as  $EPW_{(i,ii,iii)}$  (Eq. 10) when using the approxima-  
 258 tion of (iii) topographic interactions (**A2, C**) being negligible compared to the  $\beta$ -contribution  
 (**A1**), such that :

$$259 EPW_{(i,ii,iii)} = \underbrace{-\frac{\beta\rho_0g^2}{2f^2} \frac{\partial}{\partial x} \left( \frac{\int_{-H}^{\eta} \phi_1^2 dz}{|\phi_1^2|_{z=0}} \eta'^2 \right)}_{\beta\text{-contribution (A1)}} \quad (10)$$

260 The expression of  $EPW_{(i,ii,iii)}$  (Eq. 10) corresponds to the contribution of linear  $EKE$   
 261 flux, driven by the  $\beta$ -effect, acting on the 1<sup>st</sup> baroclinic mode to the true  $EPW$  (Zhai et  
 262 al., 2010).

263 We additionally define  $EPW_{(i,iii)}$  (Eq. 11), which is equivalent to  $EPW_{(i,ii,iii)}$  (Eq. 10)  
 264 with approximation (ii) relaxed, such that :

$$265 EPW_{(i,iii)} = \underbrace{-\frac{\beta\rho_0g^2}{2f^2} \frac{\partial}{\partial x} \left( \frac{\int_{-H}^{\eta} \phi_n^2 dz}{|\phi_n^2|_{z=0}} \alpha_n^2 \eta'^2 \right)}_{\beta\text{-contribution (A1)}} \quad (11)$$

266 In the following sections, we will test if  $EPW_{(i,ii,iii)}$  (Eq. 10) and  $AEKE_{(i)}$  (Eq. 8)  
 267 are reliable approximations of  $EPW$  (Eq. 4) (section 4) and  $AEKE$  (Eq. 4) (section  
 268 5), respectively. The main terms discussed in these sections are summarized in Table 1.  
 Beforehand, section 3 presents the methods and data.

## 269 3 Method

### 270 3.1 Observations and numerical model

271 We first present the observations and the regional numerical simulation used in this  
 272 study. We then assess the sensitivity of the paradigm of mesoscale eddy decay at the Ag-  
 ulhas Current region, by comparing the observed and modeled  $EPW_{(i,ii,iii)}$  (Eq. 10). The

Table 1: Summary of the true and  $\eta$ -based expressions of the eddy-pressure work ( $EPW$ ) and advection of mesoscale  $EKE$  by the total flow ( $AEKE$ ) constituting the mesoscale  $EKE$  ( $EKE_{n=0-1}$ )-flux divergence.

Acronym	Expression	Description
$EPW$ (Eq. 5)	$\nabla_H \cdot \int_{-H}^{\eta} \mathbf{u}'_n \partial'_n \phi_n^2 dz$	true mesoscale eddy-pressure work
$EPW_{(i)}$ (Eq. 7)	$\begin{aligned} & -\frac{\beta \rho_0 g^2}{2f^2} \frac{\partial}{\partial x} \left( \int_{-H}^{\eta} \frac{\phi_n^2}{ \phi_n^2 _{z=0}} \alpha_n^2 \eta'^2 dz \right) \\ & + \frac{\beta \rho_0 g^2}{2f^2} \frac{\partial H}{\partial x} \left  \frac{\phi_n^2}{ \phi_n^2 _{z=0}} \right _{z=0} \alpha_n^2 \eta'^2 \\ & + \frac{\rho_0 g^2}{2f} \nabla_H H \cdot \mathbf{k} \wedge \nabla_H \left( \frac{\phi_n^2}{ \phi_n^2 _{z=0}} \right) \alpha_n^2 \eta'^2 \Big _{z=-H}, \end{aligned}$ <p style="text-align: center;">with <math>\alpha_n = \frac{\eta'}{\eta}</math></p>	$\eta$ -based mesoscale eddy-pressure work using approximation (i)
$EPW_{(i,ii,iii)}$ (Eq. 10)	$-\frac{\beta \rho_0 g^2}{2f^2} \frac{\partial}{\partial x} \left( \int_{-H}^{\eta} \frac{\phi_n^2}{ \phi_n^2 _{z=0}} \eta'^2 dz \right)$	$\eta$ -based mesoscale eddy-pressure work using approximations (i), (ii) and (iii)
$EPW_{(i,ii)}$ (Eq. 11)	$\frac{\beta \rho_0 g^2}{2f^2} \frac{\partial}{\partial x} \left( \int_{-H}^{\eta} \frac{\phi_n^2}{ \phi_n^2 _{z=0}} \alpha_n^2 \eta'^2 dz \right), \text{ with } \alpha_n = \frac{\eta'}{\eta}$	$\eta$ -based mesoscale eddy-pressure work using approximation (i) and (iii)
$AEKE$ (Eq. 6)	$\frac{\rho_0}{2} \nabla_H \cdot \int_{-H}^{\eta} \mathbf{u}_n \phi_n \ \mathbf{u}'_n \phi_n\ ^2 dz$	true advection of mesoscale $EKE$ by the total flow
$AEKE_{(i)}$ (Eq. 8)	$\begin{aligned} & -\frac{\beta \rho_0 g}{2f^2} \int_{-H}^{\eta}  \mathbf{u}'_{g,n} \phi_n ^2 \partial x \left( \frac{\phi_n}{ \phi_n _{z=0}} \lambda_n \eta \right) dz \\ & + \frac{\beta \rho_0 g}{2} \int_{-H}^{\eta} (\mathbf{u}_{g,n} \phi_n) \cdot \nabla_H \ \mathbf{u}'_{g,n} \phi_n\ ^2 dz \\ & + \frac{\beta \rho_0 g}{2} \nabla_H H \cdot \mathbf{u}_{g,n} \phi_n \ \mathbf{u}'_{g,n} \phi_n\ ^2 \Big _{z=-H}, \end{aligned}$ <p style="text-align: center;">with <math>\lambda_n = \frac{H}{\eta}</math></p>	$\eta$ -based advection of mesoscale $EKE$ by the total flow using approximation (i)

273 term requires vertical modes (derived using a time-averaged stratification  $N^2$ ) and  $\eta$  fields.  
 274

275 **3.1.1 Observations**

276 The WOCE (World Ocean Circulation Experiment) and WOA18 (World Ocean Atlas)  
 277 climatologies provide *in situ* temperature and salinity fields at a global scale, with respec-  
 278 tive horizontal resolutions of  $1/2^\circ$  and  $1^\circ$ , for monthly compositing means (Gouretski &  
 279 Koltermann, 2004; Locarnini et al., 2018; Zweng et al., 2019). Vertical modes are derived  
 280 from the time-averaged stratification, computed from temperature and salinity provided by  
 281 both climatologies. Altimetric data are mapped on a regular  $1/4^\circ$ - and  $1/3^\circ$ -grid by AVISO  
 282 (Archiving, Validation and Interpretation of Satellite Oceanographic data) and provide  $\eta$   
 283 field for weekly compositing means at a global scale. Here we focus on a subset of data over  
 284 the Agulhas Current region ( $15^\circ\text{E}$  -  $34^\circ\text{E}$  and  $27^\circ\text{S}$  -  $40^\circ\text{S}$ ) for the 1995-2004 period.  
 285

286 **3.1.2 Numerical model**

287 A regional numerical simulation of the Agulhas Current was performed using the  
 288 Coastal and Regional CCommunity (CROCO) model. It is a free surface model, based  
 289 on ROMS (Shchepetkin & McWilliams, 2005), which solves the primitive equations in the  
 290 Boussinesq and hydrostatic approximations using a terrain following coordinate system (De-  
 291 breu et al., 2012). The simulation has a horizontal resolution of  $\text{dx} \sim 2.5 \text{ km}$  and 60 vertical  
 292 levels. It encompasses the Agulhas Current region from its source, north of the Natal Bight  
 293 ( $27^\circ\text{S}$ ), to the Agulhas Retroflection ( $\sim 37^\circ\text{S}$ ), from where it becomes the Agulhas Return  
 294 Current and flows eastward. Boundary conditions are supplied by two lower-resolution grids  
 295 ( $\text{dx} \sim 22.5 \text{ km}$  and  $7.5 \text{ km}$ , respectively covering most of the South Indian Ocean and its  
 296 western part). The surface forcing is provided by a bulk-formulation using daily relative  
 297 winds. The regional numerical simulation settings and modeled mesoscale eddy dynamics  
 298 are presented in details by Tedesco et al. (2019, 2022). Here vertical modes are derived from  
 299 the time-averaged stratification over the 1995-2004 period, computed from the modeled  
 300 temperature and salinity.

301 **3.2  $EPW_{(i,ii,iii)}$  from observations and a numerical model**

302 In order to ensure the ability of the model to reproduce a realistic mesoscale eddy  
 303 dynamics and to assess the sensitivity of the paradigm of mesoscale eddy decay at the  
 304 Agulhas Current region, we compare  $EPW_{(i,ii,iii)}$  (Eq. 10) computed from observations (as  
 305 in Zhai et al. (2010)) and from the model (Figure 1).

306 Observed and modeled  $EPW_{(i,ii,iii)}$  are in fairly good agreement across the domain of  
 307 the  $\text{dx} \sim 2.5 \text{ km}$  grid. Both  $EPW_{(i,ii,iii)}$  are most intense at the Retroflection and along  
 308 the Agulhas Return Current ( $O(0.1\text{-}0.5) \text{ W m}^{-2}$ ) and are less intense along the Agulhas  
 309 Current and in the Subgyre ( $O(0.01\text{-}0.1) \text{ W m}^{-2}$ ). However, the Agulhas Current region  
 310 – from north of the Natal Bight ( $\sim 27^\circ\text{S}$ ) to the African tip ( $\sim 37^\circ\text{S}$ ) and from the shelf  
 311 to about 150 km offshore, a typical width of western boundary currents (black region in  
 312 Figure 1) – stands out for both. In this region,  $EPW_{(i,ii,iii)}$  is almost uniformly nega-  
 313 tive and has a cumulative net negative contribution of magnitude  $O(1) \text{ GW}$ . The negative  
 314  $EPW_{(i,ii,iii)}$  along the Agulhas Current – referred to as the Western Boundary (WB) region  
 315 in the following – is consistent with the hotspot of net  $EKE$  sink in the region near the west-  
 316 ern boundary of the South Indian Ocean (poleward of  $10^\circ\text{S}$ ) suggested by Zhai et al. (2010).  
 317

318 The main discrepancy between the observed and modeled  $EPW_{(i,ii,iii)}$  is the magni-  
 319 tude of the cumulative  $EKE$  sinks in the WB region. There is roughly a twofold decrease  
 320 in the model compared to observations (Figure 1a,b,c). The magnitude difference is still

321 present when using smoothed  $\eta$ , with a length scale of 100 km, in the model to mimic the  
 322 altimetry data processing done by AVISO (Figure 1d). It indicates that the *EKE* sink in  
 323 the WB region is robust to altimetry data processing and that horizontal scales  $< O(100)$   
 324 km do not significantly contribute to the  $EPW_{(i,ii,iii)}$  term. Using different climatologies  
 325 (1/2° WOCE or 1° WOA18) and satellite altimetry data of different resolutions (1/4° or  
 326 1/3° AVISO) also does not significantly change the result (Figure 1a,b).

327

328 The magnitude difference is unlikely explained by the forcing of eddies generated in the  
 329 parent nest that would propagate in the  $dx \sim 2.5$  km grid. The grid is forced at each time  
 330 step at the boundaries by a parent grid ( $dx \sim 7.5$  km), which resolves mesoscale eddies of  
 331 scales  $< 100$  km. An explanation can be the slight underestimation of the surface *EKE*  
 332 reservoir in the  $dx \sim 2.5$  km simulation, compared to AVISO, in the Subgyre region (Figure 2  
 333 in Tedesco et al. (2022)). A weaker *EKE* reservoir can lead to a weaker spatial redistribution  
 334 of the *EKE* (*EKE* flux divergence). It is supported by the observed  $EPW_{(i,ii,iii)}$  showing  
 335 slightly larger magnitudes ( $-0.1 \text{ W m}^{-2}$ ) than the modeled  $EPW_{(i,ii,iii)}$  ( $-0.05 \text{ W m}^{-2}$ ), in  
 336 the same areas where the surface AVISO-based *EKE* is slightly larger ( $0.05 \text{ m}^2 \text{ s}^{-2}$ ) than the  
 337 modeled one ( $> 0.03 \text{ m}^2 \text{ s}^{-2}$ ). Another explanation can be the definition of the WB region.  
 338 The uniform *EKE* sink denoted by  $EPW_{(i,ii,iii)}$  has a larger extension in the observations  
 339 than in the model (Figure 1). With a typical width of western boundary currents, the WB  
 340 region fully encompasses the modeled uniform *EKE* sink, with the southern face closely  
 341 following the  $O(0) \text{ W m}^{-1}$  isoline. However, the WB region encompasses most, but not all  
 342 of the observed uniform *EKE* sink.

343 Both observed and modeled  $EPW_{(i,ii,iii)}$  are mainly negative in the WB region, showing  
 344 a net *EKE* sink. It is consistent with the paradigm of the decay of remotely-generated  
 345 mesoscale eddy at western boundaries (Zhai et al., 2010). It also ensures that the  $dx \sim 2.5$   
 346 km numerical simulation reproduces a realistic mesoscale eddy dynamics and confirms its  
 347 use to assess the  $\eta$ -based diagnostic of *EKE* flux divergence in the WB region.

## 348 4 Results I : Validity of the approximated $EPW_{(i,ii,iii)}$ and main contributions 349 to the true $EPW$

350 In this section we evaluate the  $\eta$ -based estimate of  $EPW$  ( $EPW_{(i,ii,iii)}$ ). We first  
 351 evaluate if  $EPW_{(i,ii,iii)}$  (Eq. 10) is a reliable approximation of the true  $EPW$  (Eq. 4). We  
 352 then evaluate separately the impacts of approximations (i), (ii) and (iii) (cf. section 2.1.3)  
 353 and characterize what are the main contributions to the true  $EPW$ .

### 354 4.1 Comparison between approximated $EPW_{(i,ii,iii)}$ and true $EPW$

355  $EPW_{(i,ii,iii)}$  and  $EPW$  in Figure 2 – and in all the following Figures – have been  
 356 smoothed using a 75 km-radius Gaussian kernel. Smoothed terms emphasize the large-scale  
 357 patterns driving the cumulative contributions of  $EPW$  in the WB region and ease the com-  
 358 parison with  $EPW_{(i,ii,iii)}$ . The smoothing length scale corresponds to a typical mesoscale  
 359 eddy radius at mid-latitudes, as inferred from satellite altimetry (Chelton et al., 2011). The  
 360 sensitivity of the  $EPW$  term to the smoothing length scale is presented in Appendix A.

361

362  $EPW_{(i,ii,iii)}$  and  $EPW$  strongly differ by their patterns across the whole domain and  
 363 by their cumulative contributions in the WB region (Figures 2a and b).  $EPW_{(i,ii,iii)}$  is  
 364 mainly negative in the WB region ( $-1.10 \text{ GW}$ ; Figure 2a) and  $EPW$  is mainly positive ( $0.81$   
 365  $\text{GW}$ ; Figure 2b).

366

367  $EPW$  shows contrasted net mesoscale *EKE* sources and sinks within the WB region,  
 368 consistent with the documented Agulhas Current mesoscale variability (Lutjeharms, 2006;

manuscript submitted to *JGR: Oceans*

369 Paldor & Lutjeharms, 2009; Tedesco et al., 2022). Along the northern and stable Agulhas  
370 Current branch (upstream of Port Elizabeth),  $EPW$  is negative ( $O(-0.01)$  W m $^{-2}$ ), except  
371 at the Natal Bight ( $\sim 31^{\circ}$ E) where  $EPW$  is positive and Natal Pulses are locally generated  
372 (Elipot & Beal, 2015). Along the southern and unstable current branch (downstream of Port  
373 Elizabeth),  $EPW$  is positive over the entire width of the WB region, except at the Agulhas  
374 Bank tip ( $\sim 23^{\circ}$ E) where mesoscale  $EKE$  is locally lost. The cumulative contribution of  
375  $EPW$  across the WB region is dominated by the net mesoscale  $EKE$  sources ( $EPW > 0$ ),  
376 which are the most intense along the southern current branch where mesoscale variability  
377 is high. The locally gained mesoscale  $EKE$  is transported downstream. It mainly exits the  
378 WB region by its western face toward the South-East Atlantic Ocean or entering back the  
379 South Indian Ocean following the Agulhas Return Current (vector fields in Figure 2b).

380

381 The negative  $EPW_{(i,ii,iii)}$  and the positive  $EPW$  support opposite paradigms of mesoscale  
382 eddy dynamics in the WB region. The  $\eta$ -based version is dominated by a local decay of  
383 remotely-generated mesoscale eddies, while the true version is dominated by a local genera-  
384 tion of mesoscale eddies, which are then exported downstream. It indicates that  $EPW_{(i,ii,iii)}$   
385 (Eq. 10) –  $\beta$ -contribution acting on the 1<sup>st</sup> baroclinic mode – does not represent the main  
386 contribution to the true  $EPW$  (Eq. 5). This suggests that the contribution of  $\beta$ -effect  
387 acting on the 1<sup>st</sup> baroclinic mode is counterbalanced by other dynamical processes to pro-  
388 duce a positive  $EPW$  in the WB region. We investigate in the following which of the  
389 approximations (i), (ii) and (iii) limits the  $\eta$ -based diagnostic of  $EPW$ .

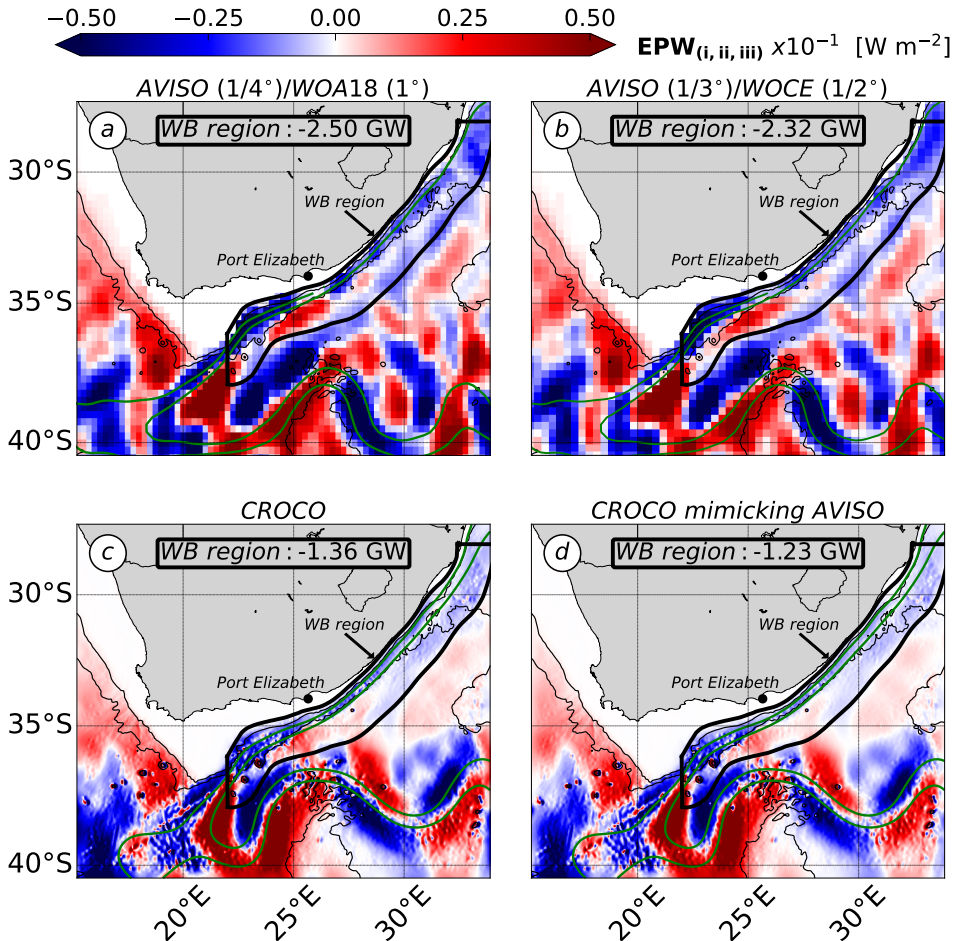


Figure 1:  $EPW_{(i,ii,iii)}$  (Eq. 10) [ $\text{W m}^{-2}$ ] for (a) AVISO new products ( $1/4^\circ$ ) and WOA18 ( $1^\circ$ ) climatology, (b) AVISO old products ( $1/3^\circ$ ) and WOCE ( $1/2^\circ$ ) climatology, (c) CROCO ( $dx \sim 2.5 \text{ km}$ ) and (d) CROCO mimicking AVISO processing ( $\eta$  fields smoothed with a 50 km-radius Gaussian kernel). Terms are averaged over the 1995–2004 period. The black area denotes the WB region and the terms integral in the region are in [GW] ( $10^9 \text{ W}$ ). The green contours denote the 0.25 m and 0.5 m isolines of time-averaged  $\eta$  and the black contours denote the 1000 m and 3000 m isobaths. (d) Small scales patterns, visible in spite of the smoothed  $\eta$  fields, are due to horizontal gradients of the 1<sup>st</sup> baroclinic mode which is at the model resolution ( $dx \sim 2.5 \text{ km}$ ). All  $EPW_{(i,ii,iii)}$  show, in good agreement, a net mesoscale EKE sink in the WB region ( $EPW_{(i,ii,iii)} < 0$ ). It is consistent with the paradigm of the decay of remotely-generated mesoscale eddies at western boundaries (Zhai et al., 2010).

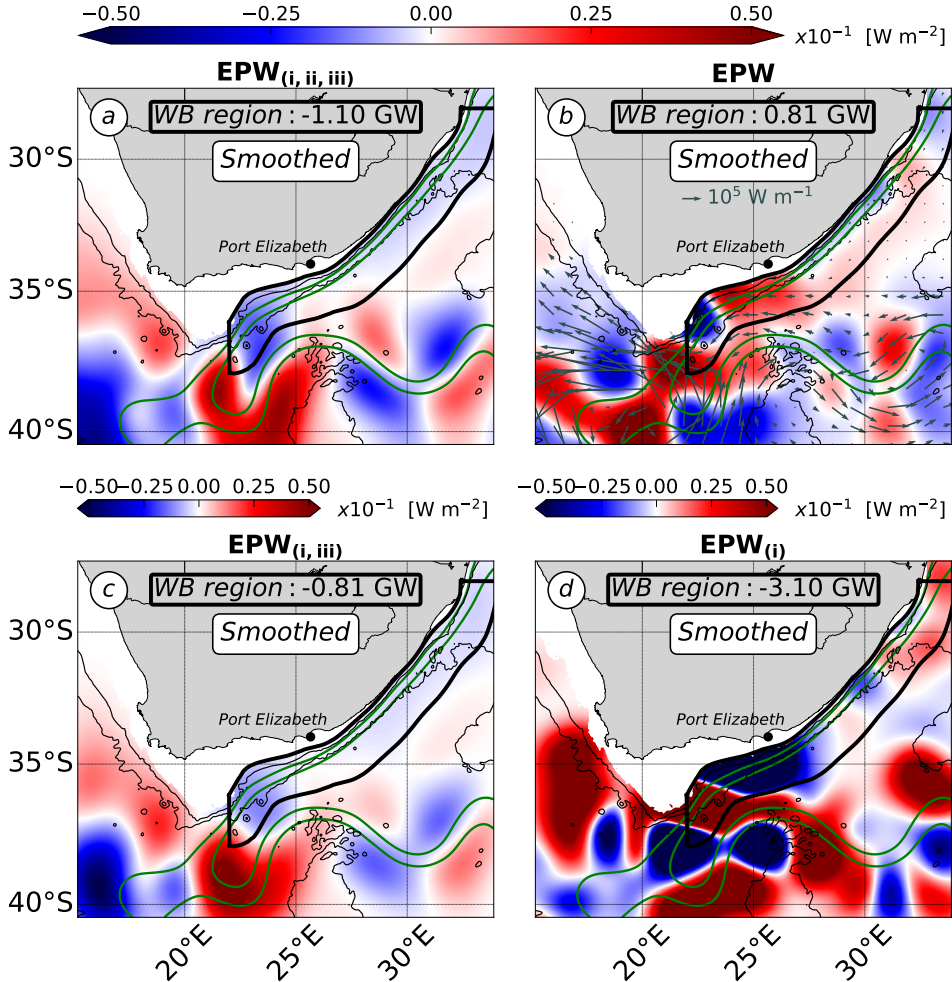


Figure 2: (a)  $EPW_{(i,ii,iii)}$  (Eq. 10), (b)  $EPW$  (Eq. 5), (c)  $EPW_{(i,iii)}$  (Eq. 11) and (d)  $EPW_{(i)}$  (Eq. 7) [ $\text{W m}^{-2}$ ]. Terms are smoothed with a 75 km-radius Gaussian kernel. (b) Vector fields denote the mesoscale  $EKE$  flux ( $\int_{-H}^{\eta} \mathbf{u}'_n p'_n \phi_n^2 dz$  with  $n = 0 - 1$ ) [ $\text{W m}^{-1}$ ] (cf. Figure 1 for a detailed caption). The black area denotes the WB region and the terms integral in this region are in [GW] ( $10^9 \text{ W}$ ). The green contours denote the 0.25 m and 0.5 m isolines of time-averaged  $\eta$  and black contours denote the 1000 m and 3000 m isobaths. (a) and (b) strongly differ ( $EPW_{(i,ii,iii)} < 0$  and  $EPW > 0$  in the WB region), indicating that  $EPW_{(i,ii,iii)}$  is not a reliable estimate of the true mesoscale  $EPW$ . (a) and (c) results from different contributions of the barotropic and 1<sup>st</sup> baroclinic modes, indicating that approximation (ii) biases the interpretation of  $EPW_{(i,ii,iii)}$ . (c) and (d) differs, invalidating approximation (iii) for the  $\eta$ -based  $EPW$ .

390        **4.2 Approximation (ii) : contribution of the barotropic mode ( $EPW_{(i,ii,iii)}$   
 391        *vs.*  $EPW_{(i,iii)}$ )**

392        With approximation (ii) ( $\eta$  field primarily reflecting the 1<sup>st</sup> baroclinic mode), the  
 393        mesoscale *EKE* reservoir – formally represented by the barotropic and 1<sup>st</sup> baroclinic modes  
 394        (Wunsch, 2007; Smith & Vallis, 2001; Venaille et al., 2011; Tedesco et al., 2022) – is repre-  
 395        sented by the 1<sup>st</sup> baroclinic mode alone. This can lead to a misinterpretation of the dynamics  
 396        of the mesoscale *EKE* reservoir. It can gain or loose *EKE* through the barotropic mode  
 397        and the barotropic and 1<sup>st</sup> baroclinic modes can exchange *EKE*, via barotropisation and  
 398        scattering processes, without affecting the content of the mesoscale *EKE* reservoir. The  
 399        importance of barotropization has been shown in the WB region of the North Indian Ocean  
 400        (Vic et al., 2014). The necessity to account for both modes to infer the mesoscale *EKE*  
 401        flux divergence in the WB region is supported by the true *EPW*. Its net contribution in  
 402        the WB region (0.81 GW; Figure 2b) results from the partial compensation between the  
 403        barotropic (1.56 GW) and the 1<sup>st</sup> baroclinic modes (-0.75 GW) (not shown), indicating that  
 404        barotropization is a significant process in the region.  
 405

406        The expression of  $EPW_{(i,iii)}$  (Eq. 11) accounts for the different vertical modes using  
 407         $\alpha_n^2$  – the vertical partitioning of the  $\eta$  variance. The  $\eta$  variance mainly partitions into the  
 408        1<sup>st</sup> baroclinic mode ( $38 \pm 2\%$ ) and more weakly, but still significantly, into the barotropic  
 409        mode ( $16 \pm 4\%$ ) (Appendix B). It indicates that the mesoscale *EKE* reservoir can be for-  
 410        mally represented by the barotropic and 1<sup>st</sup> baroclinic modes using  $\eta$ . The  $\eta$  variance also  
 411        significantly partitions into an intermodal coupling term ( $36 \pm 2\%$ ), originating from the  
 412        modal correlation in time at the surface (Wunsch, 1997). However, the intermodal coupling  
 413        term does not contribute to  $EPW_{(i,iii)}$  (Eq. 11), which uses the orthogonality contribution  
 414        (2) and only accounts for individual vertical modes.  
 415

416        Approximation (ii) is evaluated by comparing  $EPW_{(i,ii,iii)}$  (Figure 2a) with  $EPW_{(i,iii)}$   
 417        (Figure 2c).  $EPW_{(i,ii,iii)}$  and  $EPW_{(i,iii)}$  have highly similar patterns and magnitudes across  
 418        the region. However, the net mesoscale *EKE* sink in the WB region denoted by  $EPW_{(i,iii)}$   
 419        (-0.81 GW; Figure 2c) results from the combination of the barotropic (-0.51 GW) and 1<sup>st</sup>  
 420        baroclinic modes (-0.30 GW). It contrasts with the net *EKE* sink denoted by  $EPW_{(i)}$  (-1.10  
 421        GW), attributable to the 1<sup>st</sup> baroclinic mode alone (Figure 2a). This indicates that both  
 422        vertical modes are needed to accurately interpret the mesoscale *EPW*. It also indicates that  
 423        even though the barotropic mode does not dominate the  $\eta$  variance ( $16 \pm 4\%$ ; Appendix  
 424        B), it is the main contribution to the vertically-integrated  $EPW_{(i,iii)}$  in the WB region.  
 425

426        Approximation (ii) biases the interpretation of the  $\eta$ -based *EPW* ( $EPW_{(i,ii,iii)}$ ) in Eq.  
 427        10), because the barotropic mode represents the main contribution to the net *EKE* sink  
 428        in the WB region denoted by  $EPW_{(i,iii)}$  (Eq. 11). However, it is not at the origin of the  
 429        strong discrepancies between the  $\eta$ -based terms -  $EPW_{(i,ii,iii)}$  (Eq. 10) and  $EPW_{(i,iii)}$  (Eq.  
 430        11) - and the true *EPW* (Eq. 4).

431        **4.3 Approximation (iii) : contribution of topographic interactions ( $EPW_{(i,iii)}$   
432        *vs.*  $EPW_{(i)}$ )**

433        The WB region is characterized by large topographic variations, having a spatially-  
434        averaged magnitude of  $3 \cdot 10^{-2}$ , which can locally peak at  $6 \cdot 10^{-2}$ . This questions the use of  
435        approximation (iii) of *EKE* flux-topographic interactions to be negligible in the WB region.  
436

437        Approximation (iii) is evaluated by comparing  $EPW_{(i,iii)}$  (Eq. 11; Figure 2c) against  
438         $EPW_{(i)}$  (Eq. 7; Figure 2d) which includes topographic interactions. The two terms locally  
439        differ by their patterns and magnitudes. However, their cumulative contributions in the  
440        WB region show a net mesoscale *EKE* sink ( $EPW_{(i,iii)}; EPW_{(i)} < 0$ ).  $EPW_{(i)}$ , including  
441        topographic interactions, has contrasted patterns within the WB region and is the most  
442        intense at the Eastern Agulhas Bank Bight ( $23^{\circ}\text{E}-27^{\circ}\text{E}$ ). Its local magnitude is larger by an  
443        order of magnitude than that of  $EPW_{(i,iii)}$ , excluding topographic interactions.  
444

445        Topographic interactions are mainly due to the term of *EKE* flux-topographic interactions (**C** : -3.05 GW in the WB region, not shown), because the term of  $\beta$ -contribution  
446        to topographic interactions has a negligible contribution (**A2** : 0.76 GW in the WB region,  
447        not shown). A valid approximation would be to neglect the  $\beta$ -contribution (**A1**) and the  $\beta$ -  
448        contribution to the topographic interactions (**A2**) compared to the *EKE* flux-topographic  
449        interactions (**C**).  
450

451        Approximation (iii) has a significant impact on  $EPW_{(i,iii)}$  (Eq. 11). However,  $EPW_{(i)}$   
452        (Eq. 7) – adjusted of approximations (ii) and (iii) – is mainly negative in the WB region,  
453        consistently with the former version of the  $\eta$ -based *EPW* ( $EPW_{(i,ii,iii)}$  in Eq. 10). It  
454        indicates that approximations (ii) and (iii) are not the reasons for the opposite signs in the  
455        WB region between the  $\eta$ -based ( $EPW_{(i,ii,iii)}$  in Eq. 10; Figure 2a) and the true *EPW*  
456        (*EPW* in Eq. 4; Figure 2b).  
457

458        **4.4 Approximation (i) : contribution of ageostrophic motions ( $\beta$ -contribution  
459        *vs.* ageostrophic *EPW*)**

460        Approximation (i) of geostrophic velocities is the last possible reason for the opposite  
461        signs of the  $\eta$ -based ( $EPW_{(i,iii)}, EPW_{(i)} < 0$ ; Figure 2c,d) and true *EPW* ( $EPW > 0$ ;  
462        Figure 2b) in the WB region. It suggests that the main contribution to the true mesoscale  
463        *EPW* is the ageostrophic part of mesoscale eddies velocity.  
464

465        We use a scale analysis to explain the prevalence of ageostrophy, compared to the  $\beta$ -  
466        contribution (in  $EPW_{(i)}$ ; Eq. 7 and  $EPW_{(i,iii)}$ ; Eq. 11), for the true *EPW* (Eq. 4).  
467        We focus here on the  $\beta$ -contribution only, because it was the one investigated as the main  
468        contribution to the true *EPW* by Zhai et al. (2010). The decomposition of velocity and  
469        pressure into a geostrophic and an ageostrophic part in the modal *EKE* equation (Eq. 4),  
470        results in three types of contribution to *EPW*: a purely geostrophic one ( $\beta$ -contribution  
471        to  $EPW_i$ ; Eq. 7), a purely ageostrophic one ( $\mathbf{u}'_{ag,n}; p'_{ag,n}$ ), and a coupled geostrophic-  
472        ageostrophic one ( $\mathbf{u}'_{ag,n}; p'_{g,n}$ ). We derive the scale analysis for the purely ageostrophic (Eq.  
473        12) and partially ageostrophic (Eq. 13) terms to assess their contribution to the true *EPW*.

$$\left| \int_{-H}^H \nabla_H \cdot (\mathbf{u}'_{ag,n} p'_{ag,n} \phi_n^2) dz \right| \sim \frac{Ro^2 U'_g P'_g H}{L} \quad (12)$$

$$\left| \int_{-H}^H \nabla_H \cdot (\mathbf{u}'_{ag,n} p'_{g,n} \phi_n^2) dz \right| \sim \frac{Ro U'_g P'_g H}{L} \quad (13)$$

$$\left| \frac{\beta \rho_0 g^2}{2f^2} \int_H^\eta \frac{\partial}{\partial x} \left( \frac{\phi_n^2}{|\phi_n^2|_{z=0}} \alpha_n^2 \eta'^2 \right) dz \right| \sim \frac{\widehat{\beta} P' U'_g H}{\widehat{f}} \quad (14)$$

$$\frac{(12)}{(14)} = \frac{Ro^2 \widehat{f}}{L \widehat{\beta}} = \frac{\widehat{\zeta}_{RMS}^2}{L \widehat{f} \widehat{\beta}} = \frac{L_{cross-over}}{L}, \text{ with } L_{cross-over} = \frac{\widehat{\zeta}_{RMS}^2}{\widehat{f} \widehat{\beta}} \quad (15)$$

$$\frac{(13)}{(14)} = \frac{Ro \widehat{f}}{L \widehat{\beta}} = \frac{\widehat{\zeta}'_{RMS}^2}{L \widehat{\beta}} = \frac{L_{cross-over}}{L}, \text{ with } L_{cross-over} = \frac{\widehat{\zeta}'_{RMS}^2}{\widehat{\beta}} \quad (16)$$

with  $|\nabla_H \frac{\partial}{\partial x}| \sim \frac{1}{L}$ ,  $|\int_{-H}^\eta < . > dz| \sim H$ ,  $|\beta| \sim \widehat{\beta}$ ,  $|f| \sim \widehat{f}$ ,  $|\mathbf{u}'_{ag,n}| \sim Ro U'_g$  and  $|p'_{ag,n}| \sim Ro P'_g$  using the expansion of velocity and eddy pressure with  $Ro$  the small parameter – defined as the vertical average of the root mean square of the normalized relative vorticity of mesoscale eddies ( $\zeta' = \partial_x v' - \partial_y u'$ ), such as :  $Ro = \left| \frac{1}{H} \int_{-H}^H \left( \frac{\zeta'_{RMS}}{f} \right) dz \right| \sim \frac{\widehat{\zeta}_{RMS}}{\widehat{f}}$  –  $|p'_{g,n}| \sim P'_g \sim \rho_0 \widehat{f} U'_g L$  using geostrophy and  $\left| \frac{\phi_n^2 \alpha_n^2 \eta'^2}{|\phi_n^2|_{z=0}} \right| \sim \frac{P'_g U'_g L \widehat{f}}{\rho_0 g^2}$  using the hydrostatic approximation and geostrophy.

480

The scale analysis leads to the definition of a cross-over scale ( $L_{cross-over}$  in Eq. 15 and 16) marking the transition from an ageostrophic-dominated EPW ( $L_{cross-over} \gg L_{eddy}$ ) to a  $\beta$ -effect dominated EPW ( $L_{cross-over} \ll L_{eddy}$ ). It must be noted that the definition of  $L_{cross-over}$  is not unique. An equivalent expression can be obtained by using  $Ro = \frac{U'}{fL}$ , such that :  $\frac{(13)}{(14)} = \frac{U'}{L^2 \widehat{\beta}} = \frac{L_{cross-over}^2}{L^2} = \sqrt{\frac{U'}{\widehat{\beta}}} = Rh$ .  $Rh$  is the Rhines scale defined in turbulence geostrophic theory to mark the transition from an advectively-dominated ( $Rh \ll L_{eddy}$ ) to a Rossby waves-dominated ( $Rh \gg L_{eddy}$ ) turbulent regime (Rhines, 1975). We discuss here  $Ro = \frac{\zeta'_{RMS}}{f}$  (Figure 3a) and the corresponding scale ratio  $\frac{L_{cross-over}}{L}$  (Eq. 12; Figure 3b and Eq. 13; not shown).  $Rh$  is assessed for comparison in Appendix C.

491

$Ro$  is a measure of ageostrophy (Cushman-Roisin & Beckers, 2011). The typical range of  $Ro$  values for mesoscale eddies at mid-latitudes, inferred from satellite altimetry data ( $O(< 0.05)$  from Chelton et al. (2011)), is used as a reference for mesoscale eddies in the WB region.  $Ro$  has a contrasted distribution in the WB region (Figure 3a). 70 % of its values are in the range  $O(0.02 - 0.07)$ . The rest of the values are larger ( $O(0.07-0.65)$ ) and located at the Agulhas Current inner front. It confirms that mesoscale eddies are mainly geostrophic in most of the WB region. They are more ageostrophic at the inner front where the velocity shear is more intense and where they likely interact with topography.

500

Although geostrophy is a good approximation for mesoscale eddies velocity in most of the WB region (Figure 3a), the purely geostrophic EPW – corresponding to a  $\beta$ -contribution (Figures 2a,c) – is not the main contribution to the true mesoscale EPW (Figures 2b). For the case of a partially ageostrophic EPW ( $L_{cross-over}$  in Eq. 13),  $L_{cross-over} \sim O(3-7)Rd$  in 70 % of the WB region, with larger ratio ( $L_{cross-over} \sim O(7-19)Rd$ ) located at the inner front of the Agulhas Current (Figure 3b). It indicates that the partially ageostrophic EPW dominates the  $\beta$ -effect for the mesoscale regime in the WB region. The partially ageostrophic-dominated EPW is also supported by the equivalent expression of  $L_{cross-over}$  depending on  $Rh$  (Appendix C). A typical radius of mesoscale eddies at mid-latitudes, inferred by satellite altimetry, is 75 km (Chelton et al., 2011). With  $L_{cross-over} = O(105-$

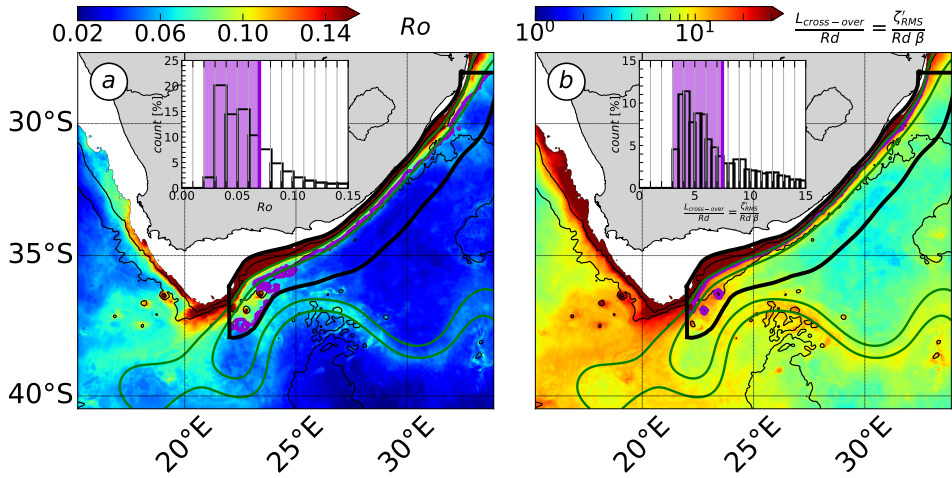


Figure 3: (a)  $Ro$  for mesoscale eddies ( $Ro = \frac{\zeta'_{RMS}}{f}$ , with  $\zeta'$  the normalized relative vorticity) and (b)  $\frac{L_{cross-over}}{Rd} = \frac{\zeta'_{RMS}}{Rd \beta}$  defined for the partially ageostrophic EPW (Eq. 16). The purple lines denote  $Ro$  and  $\frac{L_{cross-over}}{Rd}$  70 % percentiles, the green contours denote the 0.25 m and 0.5 m isolines of time-averaged  $\eta$  and black contours denote the 1000 m and 3000 m isobaths. The terms count in the WB region [%] are shown as barplots, where purple shaded areas denote the 70 % percentile range of values. (a)  $Ro$  shows that mesoscale eddies are mainly geostrophic in the WB region ( $O(0.02-0.07)$  in 70 % of the WB region). However, (b)  $\frac{L_{cross-over}}{Rd} >> 1$  in the WB region, resulting in  $L_{eddy}$  ( $\geq Rd$ ) to fall in the range of partially ageostrophic-dominated EPW, compared to the  $\beta$ -effect.

256) km in 70 % of the WB region (not shown), the  $\beta$ -effect would be the main contribution to the true mesoscale EPW for the large-scale range of mesoscale eddies. For the case of a purely ageostrophic EPW ( $L_{cross-over}$  in Eq. 12),  $L_{cross-over} \sim O(0.1 - 0.5)Rd$  in 70 % of the WB region with larger ratio located at the inner front of the Agulhas Current (not shown). It indicates that the  $\beta$ -effect dominates the purely ageostrophic EPW for the mesoscale regime in the WB region.

In a nutshell, the main contribution to the true mesoscale EPW takes the form of a coupled geostrophic (pressure) and ageostrophic (velocity) EPW in the WB region ( $L_{cross-over} >> L_{eddy}$  from Eq. 13). Approximation (i) therefore questions the use of satellite altimetry data to infer EPW (Eq. 5). In order to conclude on the use of satellite altimetry data to infer the EKE flux divergence, we assess in the following section the impact of the geostrophic approximation (i) on the AEKE term.

523      **5 Results II : Main contributions to the true  $AEKE$**

524      In this section we evaluate the  $\eta$ -based estimate of  $AEKE$  ( $AEKE_{(i)}$ ). We first evaluate  
 525      if  $AEKE_{(i)}$  (Eq. 8) is a reliable approximation of  $AEKE$  (Eq. 4). We then characterize  
 526      the main contributions to the true  $AEKE$ .

527      **5.1 Comparison between approximated  $AEKE_{(i)}$  and true  $AEKE$**

528       $AEKE_{(i)}$  and  $AEKE$  are in fairly good agreement across the whole domain (Figure  
 529      4a,b). They are mainly positive in the WB region, supporting the WB region as the place  
 530      of mesoscale eddy generation whose energy is then exported. Both  $AEKE$  are the most  
 531      intense along the southern Agulhas Current branch (downstream of Port Elizabeth), where  
 532      mesoscale variability is high. Along this portion of the current, the net mesoscale  $EKE$   
 533      sources spread almost uniformly across the width of the WB region. The net mesoscale  
 534       $EKE$  source cumulated in the WB region shown by  $AEKE_{(i)}$ , amounts to 73 % of the one  
 535      shown by  $AEKE$ . The weaker magnitude is explained by the presence of a large sink at  
 536      the Eastern Agulhas Bank Bight Tip (22°E - 23°E) visible in  $AEKE_{(i)}$ .

537      The fairly good qualitative and quantitative agreements between  $AEKE_{(i)}$  and the true  
 538       $AEKE$  indicate that the  $\eta$ -based term is a reliable estimate of  $AEKE$ . It subsequently  
 539      indicates that the approximation (i) of geostrophy is valid for  $AEKE$ , in contrast with  
 540       $EPW$  (section 4.4) and consistently with  $Ro$  (Figure 3a). In the following subsection, we  
 541      characterize in details the contribution of each sub-components –  $\beta$ -contribution (**A** in Eq.  
 542      8), work of eddy-total flow interactions (**B** in Eq. 8) and  $EKE$  flux-topographic interactions  
 543      (**C** in Eq. 8) – to  $AEKE_{(i)}$  (Eq. 8).

544      On a separate note, both terms result from a combination of the barotropic ( $AEKE_{(i)}$   
 545      : 0.57 GW ;  $AEKE$  : 0.88 GW, not shown) and 1<sup>st</sup> baroclinic modes ( $AEKE_{(i)}$  : 1.10 GW  
 546      ;  $AEKE$  : 1.41 GW, not shown). It confirms the need to consider both vertical modes to  
 547      accurately infer the mesoscale  $EKE$  flux divergence in the WB region.

548      **5.2 Approximation (i) : contribution of geostrophic motions to the true  
 549       $AEKE$**

551      The work of eddy-total flow interactions (**B** in Figure 4d) represents the main contribu-  
 552      tion to  $AEKE_{(i)}$  (Figure 4a) and the  $\beta$ -contribution (**A** in Figure 4c) has a weaker and  
 553      opposite contribution.

554      The work of eddy-total flow interactions (**B** in Eq. 8) is a reliable estimate of the net  
 555      mesoscale  $EKE$  source in the WB region denoted by  $AEKE_{(i)}$  (up to 73 %) and by  $AEKE$   
 556      (up to 53 %). The  $\beta$ -contribution (**A** in Eq. 8) is almost uniformly negative in the WB  
 557      region and amounts for a cumulated net mesoscale  $EKE$  sink of -0.19 GW. **A** in  $AEKE$   
 558      (Eq. 8) is the nonlinear counterpart of the  $\beta$ -contribution to  $EPW$  (**A** term in Eq. 7).  
 559      Both  $\beta$ -terms have similar contributions to the  $EKE$  flux divergence (Figures 2c and 4c),  
 560      although the nonlinear  $\beta$ -term has a weaker cumulative contribution in the WB region (-0.19  
 561      GW; Figure 4c) than the linear  $\beta$ -term (-0.81 GW; Figure 2c). The cumulative contribution  
 562      in the WB region of  $EKE$  flux-interactions with topography (**C** in Eq. 8) is 0.65 GW  
 563      (not shown). It is weaker than the work of eddy-total flow interactions (**B**), but remains  
 564      significant. It confirms the need to account for topographic interactions to accurately infer  
 565      the net mesoscale  $EKE$  sources and sinks in the WB region.

566

## 568 6 Conclusion on the $\eta$ -based *EKE* flux divergence

569 In this section, we draw a conclusion on the use of  $\eta$  to infer the *EKE* flux divergence,  
 570 based on our results for the *EPW* (cf. section 4) and *AEKE* components (cf. section 5).

572 The *EKE* flux divergence shows a net mesoscale *EKE* source in the WB region  
 573 ( $EPW > 0$  in Figure 2b;  $AEKE > 0$  in Figure 3b), supporting the WB as a region of  
 574 mesoscale eddies generation. The net mesoscale *EKE* source in the WB region (3.10 GW)  
 575 is mainly due to *AEKE* (2.29 GW) and more weakly to *EPW* (0.81 GW).

576

577 *AEKE* corresponds to the advection of *EKE* by the total flow. It significantly exports  
 578 *EKE* along the southern Agulhas Current branch ( $AEKE > 0$ ), where mesoscale variabil-  
 579 ity is high (Figure 4b). *AEKE* is dominated by geostrophic *EKE* flux (73 % in the WB  
 580 region; Figure 4a), in the form of the work of eddy-total flow interactions (53 % in the WB  
 581 region; Figure 4d). *EPW* represents *EKE* transport done by the linear part of variability,  
 582 usually interpreted as the wave dynamics. Its cumulated contribution in the WB region  
 583 is dominated by the *EKE* export along the southern current branch ( $EPW > 0$ ), where  
 584 mesoscale variability is high. *EPW* is dominated by the coupled geostrophic-ageostrophic  
 585 *EKE* flux. A scaling analysis (Eq. 16) shows that for typical mesoscale eddies dynamics in  
 586 the WB region, the partially ageostrophic *EPW* dominates the geostrophic *EPW* due to  
 587 the  $\beta$ -effect.

588

589 The geostrophic approximation is required by the use of  $\eta$  and is the most critical ap-  
 590 proximation to infer the *EKE* flux divergence. In the WB region, the approximation is  
 591 valid for the *AEKE* component, which dominates the *EKE* flux divergence. The use of  
 592  $\eta$  to infer the *EKE* flux divergence therefore leads to a fairly good qualitative degree of  
 593 accuracy, even if it significantly underestimates its magnitude in the WB region (46 %).

594

595 Approximations (ii) ( $\eta$  primarily reflecting the 1<sup>st</sup> baroclinic mode) and (iii) (weak  
 596 topographic interactions) are less critical, but significantly bias the interpretation and ac-  
 597 curacy of the *EKE* flux divergence. Both approximations are not directly required by the  
 598 use of  $\eta$  field and can potentially be relaxed using other datasets in addition to satellite  
 599 altimetry data. Numerical outputs and bathymetry data would respectively be needed to  
 600 derive  $\eta$  partitioning between vertical modes (approximation (ii)) and the contribution of  
 601 the *EKE* flux-topographic interactions (approximation (iii)).

## 602 7 Summary and Discussion

### 603 7.1 Summary

604 We have assessed the mesoscale *EKE* flux divergence in the region of the Agulhas  
 605 Current as well as the use of sea surface height ( $\eta$ ) to infer it, using a numerical simulation.  
 606 The  $\eta$ -based *EKE* flux divergence is a reliable qualitative estimate of the true one (54 %),  
 607 via one of its component – the advection of *EKE* by the total flow (*AEKE*; Figure 4). It  
 608 is in favor of the use of satellite altimetry data to infer the net mesoscale *EKE* sources and  
 609 sinks in the region of the Agulhas Current.

610

### 611 7.2 Discussion

612 Our study supports the WB region of the Agulhas Current as a hotspot of mesoscale  
 613 eddy generation, whose energy is then exported (*EKE* flux divergence  $> 0$ ; Figures 2b  
 614 and 4b). It is in contrast with the paradigm of the decay of remotely-generated mesoscale

615 eddies at western boundaries ( $EKE$  flux divergence  $< 0$ ), likely due to direct  $EKE$  routes  
 616 channeled by topography (Zhai et al., 2010; Chelton et al., 2011; Evans et al., 2020; Z. Yang  
 617 et al., 2021; Evans et al., 2022).  
 618

619 The latter paradigm relies on the  $\beta$ -effect being the main contribution to the  $EKE$   
 620 flux divergence (Zhai et al., 2010). Our analysis shows that this contribution is weak for  
 621 the mesoscale regime in the WB region, explaining the different paradigms. The weak  
 622  $\beta$ -contribution is assessed using a scale analysis. In the WB region, the typical scale of  
 623 mesoscale eddies falls in the range of a partially ageostrophic-dominated  $EPW$ , compared  
 624 to the purely geostrophic  $EPW$ , which reduces to the  $\beta$ -contribution (Eq. 13; Figure 3b  
 625 dn Appendix C). In the WB region, purely geostrophic flows – others than the  $\beta$ -effect –  
 626 contribute significantly to the  $EKE$  flux divergence, via  $AEKE$  (nonlinear component).  
 627 The scale analysis shows the sensitivity of the  $EKE$  flux divergence to metrics set by the  
 628 regional mesoscale dynamics. It can vary within western boundary regions across latitudes  
 629 and across oceanic gyres, possibly pointing toward opposite contributions to the  $EKE$  flux  
 630 divergence. The paradigm of the decay of remotely-generated mesoscale eddies may there-  
 631 fore be valid in specific oceanic regions.  
 632

633 The leading order processes of the mesoscale  $EKE$  budget in western boundary regions  
 634 allow to further interpret the mesoscale  $EKE$  flux divergence. In the Agulhas Current, a  
 635 study showed that the mainly positive mesoscale  $EKE$  flux divergence results from the local  
 636 generation of  $EKE$  by instability processes of the current, overcoming the local  $EKE$  decay  
 637 by topographically-channeled interactions and dissipation due to bottom-friction and wind  
 638 (Tedesco et al., 2022). It is in contrast with studies at a mid-latitude western boundary,  
 639 free of a western boundary current, which showed that the decay of remotely-generated  
 640 mesoscale eddies is due to a zoo of topographically-channeled processes triggering direct  
 641  $EKE$  routes to dissipation (Evans et al., 2020, 2022). In the same way, a study simulating  
 642 an idealized western boundary, free of a mean current, showed a mesoscale eddies decay due  
 643 to topographically-channeled turbulence in the presence of rough topography (Z. Yang et  
 644 al., 2021). The different studies suggest that in the presence of an intense mean current,  
 645 the local generation of  $EKE$  may overcome the local decay, while in the absence of intense  
 646 generation processes, the local  $EKE$  decay will likely dominate.  
 647

648 In a nutshell, the different studies suggest that, western boundary regions would be the  
 649 place of contrasted mesoscale  $EKE$  flux divergence depending on regional factors. However,  
 650 the validity of our discussion in the context of other WB regions is to consider cautiously,  
 651 as the different studies are based in different western boundary regions and use different  
 652 methods. It would require additional studies of other western boundary regions, including or  
 653 excluding a mean current, to conclude on the western boundary regions dynamics and their  
 654 contributions to the global ocean energy budget. Some elements of response on mesoscale  
 655 eddy dynamics generic to western boundaries can be found using numerical simulations  
 656 (Qiu et al., 2018; Torres et al., 2018). The SWOT mission presents the potential to test at  
 657 a global scale the suggestion that western boundaries have contrasted contributions to the  
 658 global ocean energy budget.

**659 Appendix A Sensitivity of the true *EPW* to spatial smoothing**

660 The true *EPW* (Eq. 4) is spatially smoothed to emphasize the large-scale patterns  
661 driving its cumulative contribution in the WB region.

662 The unsmoothed *EPW* term is characterized by small-scales patterns that are the most in-  
663 tense at topographic features – shelf slope (1000 m isobath), seamounts, canyons, roughness,  
664 etc – locally peaking at  $O(2.5 - 10)$  W m<sup>-2</sup> (Figure A1a). The intense small-scales patterns  
665 are larger by an order of magnitude than the unsmoothed  $EPW_{(i,ii,iii)}$  term in the WB  
666 region ( $O(0.001-0.1)$  W m<sup>-2</sup>; Figure 2a). However, *EPW* has a cumulative contribution in  
667 the WB region (1.31 GW; Figure A1a) close to the one of  $EPW_{(i,ii,iii)}$  (-1.33 GW; Figure  
668 2a), regardless of the intense small-scale patterns. It indicates that the intense small-scale  
669 patterns locally compensate and do not significantly contribute to the *EPW* cumulative  
670 contribution in the WB region.

671

672 The sensitivity of the true *EPW* (Eq. 4) to the smoothing is shown using a Gaussian  
673 kernel of progressively increasing length scale : from 35 km, the spatially-averaged *Rd* over  
674 the dx ~ 2.5 km grid, to 50 km and to 75 km, two typical mesoscale eddies radii at mid-  
675 latitudes as inferred from satellite altimetry (Chelton et al., 2011) (Figure A1). While the  
676 patterns of *EPW* significantly change with the different smoothing length scales, the order  
677 of magnitude of the cumulative contribution in the WB is fairly unchanged.

678 In the Figures of the present study, the label 'smoothed' refers to the Gaussian kernel us-  
679 ing a 75 km-radius. Both smoothings, using a 50 km- or a 75 km-radius, result in fairly  
680 close cumulative *EPW* contributions in the WB region (Figures A1c,d). The 75 km-radius  
681 smoothing provides smoother patterns, emphasizing the most the large-scale patterns driv-  
682 ing the *EPW* cumulative contribution in the WB region and easing the most its comparison  
683 with  $EPW_{(i,ii,iii)}$  (Eq. 10).

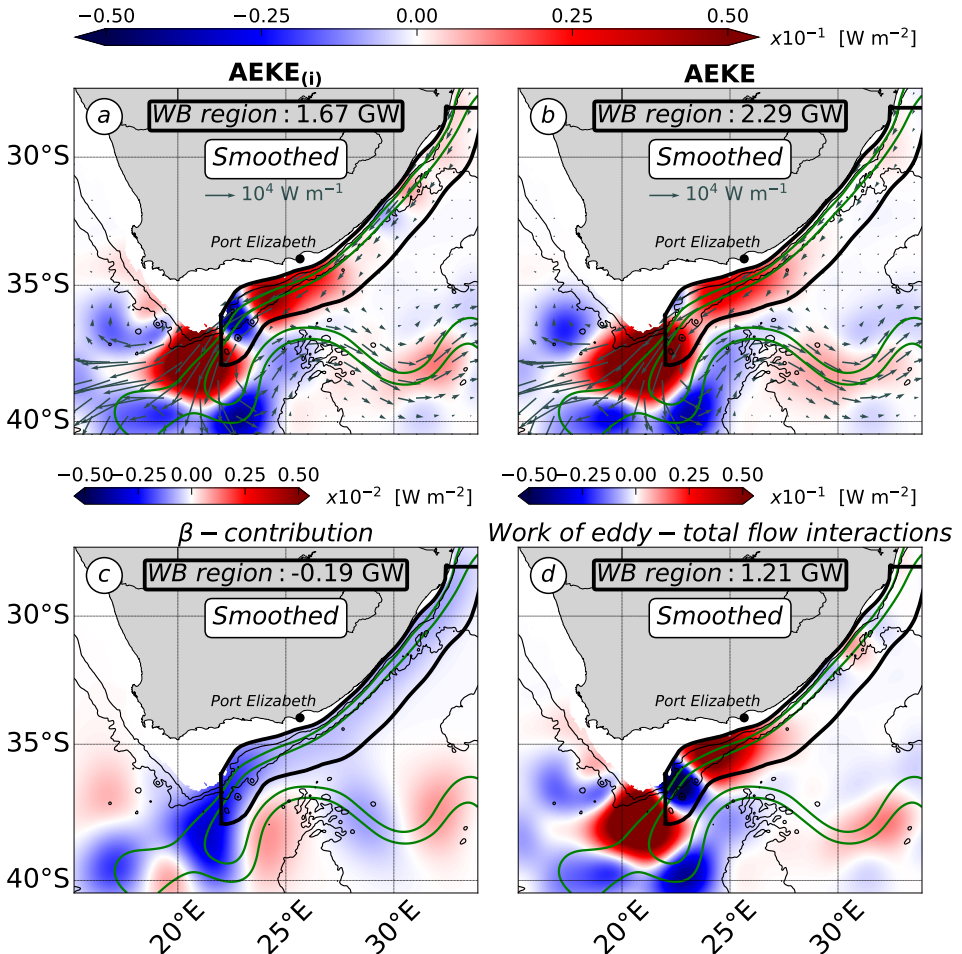


Figure 4: (a)  $AEKE_{(i)}$  (Eq. 8), (b)  $AEKE$  (Eq. 6), (c)  $\beta$ -contribution (**A**) to  $AEKE_{(i)}$  and (d) contribution of work of the eddy-total flows interactions (**B**) to  $AEKE_{(i)}$  [ $W m^{-2}$ ]. Terms are smoothed using a 75 km-radius Gaussian kernel. Note the magnitude difference between (a,b,d) and (c). (a,b) Vector fields denote the  $EKE$  flux ( $\frac{\rho_0}{2} \int_{-H}^{\eta} \mathbf{u} \phi_n ||\mathbf{u}'_n \phi_n||^2 dz$  with  $n = 0 - 1$ ) using (a) geostrophic ( $\mathbf{u}_{n,g} \phi_n = \mathbf{k} \wedge \frac{g}{f} \nabla_H \left( \frac{\phi_n}{|\phi_n|} \lambda_n \eta \right)$  with  $\lambda_n = \frac{\eta_n}{\eta}$ ) and (b) total velocity fields ( $\mathbf{u}_n \phi_n$ ) [ $W m^{-1}$ ]. (cf. Figure 1 for a detailed caption). (a)  $AEKE_{(i)}$  is dominated by (d) the work of eddy-total flows interactions and is a reliable estimate of (b) the true mesoscale  $AEKE$ .

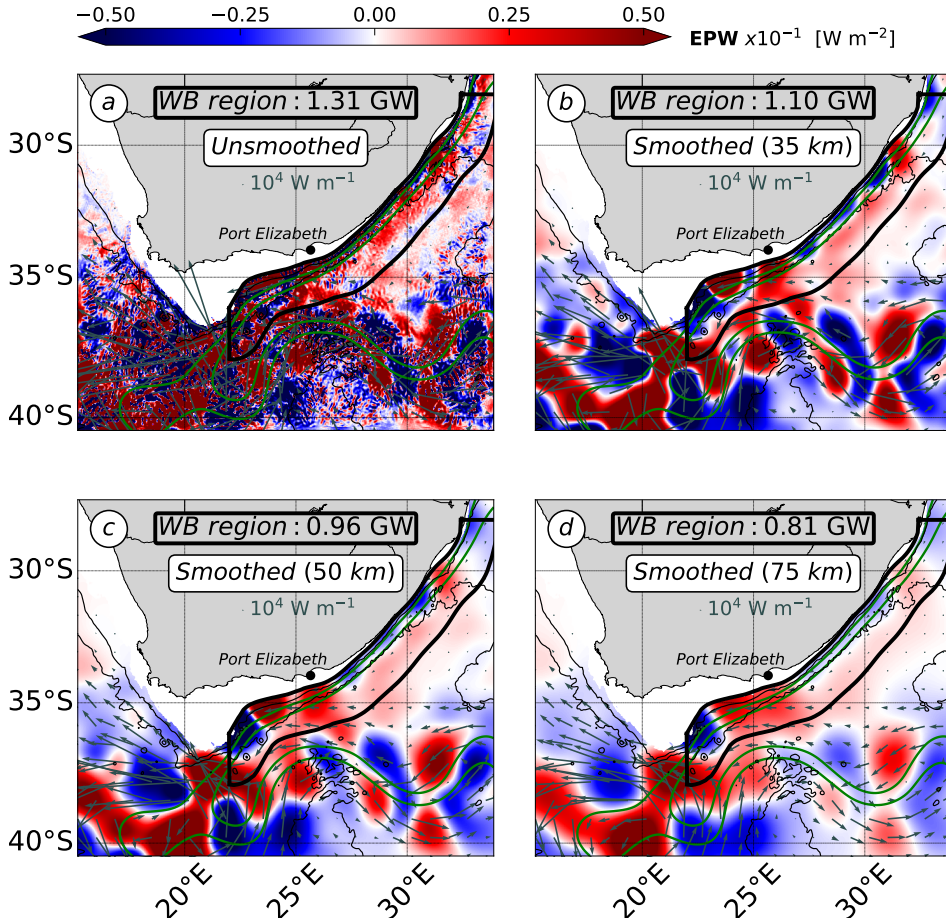


Figure A1: (a) Unsmoothed and (b,c,d) smoothed true mesoscale EPW terms (Eq. 5) [ $\text{W m}^{-2}$ ]. The radius of the Gaussian kernel used for smoothing varies from (b) 35 km, (c) 50 km to (d) 75 km. Vector fields denote the EKE flux ( $\int_{-H}^{\eta} \mathbf{u}' p'_n \phi_n^2 dz$  with  $n = 0 - 1$ ) [ $\text{W m}^{-1}$ ]. (cf. Figure 1 for a detailed caption). (d) The 75 km-radius smoothing length scale, a typical radius of mesoscale eddy at mid-latitudes (Chelton et al., 2011), emphasizes the large-scale patterns driving the cumulative contribution of the true EPW in the WB region and eases its comparison with  $\text{EPW}_{(i,ii,iii)}$  (Eq. 10; Figure 1c).

684  
685

## Appendix B Partitioning of $\eta$ variance between the barotropic and 9 first baroclinic modes

The partitioning of the  $\eta$  variance ( $\eta'^2$ ) between the vertical modes ( $\alpha_n^2$ ) is used to define  $EPW_{(i,iii)}$  (Eq. 11), an adjusted expression of  $EPW_{(i,ii,iii)}$  (Eq. 10), in order to evaluate approximation (ii) of  $\eta$  field primarily reflecting the 1<sup>st</sup> baroclinic mode (section 2.1.3.2).

We limit our analysis to the barotropic and 9 first baroclinic modes which capture 85-100 % of the modeled  $\eta'^2$  in the Agulhas Current region (not shown).  $\eta$  is a 2D field and cannot be projected on the vertical mode base  $\phi_n$ , but the  $\eta$  modal coefficient ( $\eta_n$ ) is inferred using the relation  $|p|_{z=0} = \rho_0 g \eta$ , as follows :  $\eta_n = \frac{1}{\rho_0 g} \frac{p_n}{|\phi_n|_{z=0}}$ . The modal expression of  $\eta'^2$  is derived and  $\alpha_n^2$  defined as follows :

$$\eta'^2 = \sum_{n=0}^{\infty} \eta'_n \sum_{m=0}^{\infty} \eta'_m = \sum_{n=0}^{\infty} \eta'^2_n + \underbrace{\sum_{n=0}^{\infty} \sum_{m \neq n} \eta'_n \eta'_m}_{\text{Intermodal coupling } (C_{nm})} = \sum_{n=0}^{\infty} \eta'^2_n + C_{nm} \quad (\text{B1})$$

$$\alpha_n^2 = \frac{\eta'^2_n}{\eta'^2} ; \alpha_{nm} = \frac{C_{nm}}{\eta'^2} \quad (\text{B2})$$

686  
687  
688  
689  
690  
691  
692  
693

The modal expression of  $\eta'^2$  involves an intermodal coupling term  $C_{nm}$  (B1). It corresponds to a phase-locked combination of vertical modes due to the modal correlation in time at the surface (Wunsch, 1997; Scott & Furnival, 2012). The degree of the modeled modal correlation at the surface ( $\frac{\sum_{n=0}^9 \eta'^2_n}{\sum_{n=0}^9 \eta'^2_n + C_{nm}}$ ) is 1.8 in average in the Agulhas Current region, which is consistent with the 2-3 factor determined from *in situ* data at global-scale by Wunsch (1997). It must be noted that the true  $EPW$  (Eq. 5) implies the orthogonality condition (resulting in canceling out the  $C_{nm}$  term) and that it therefore only accounts for the contributions of the individual vertical modes categories ( $n = 0$  and  $n = 1$ ).

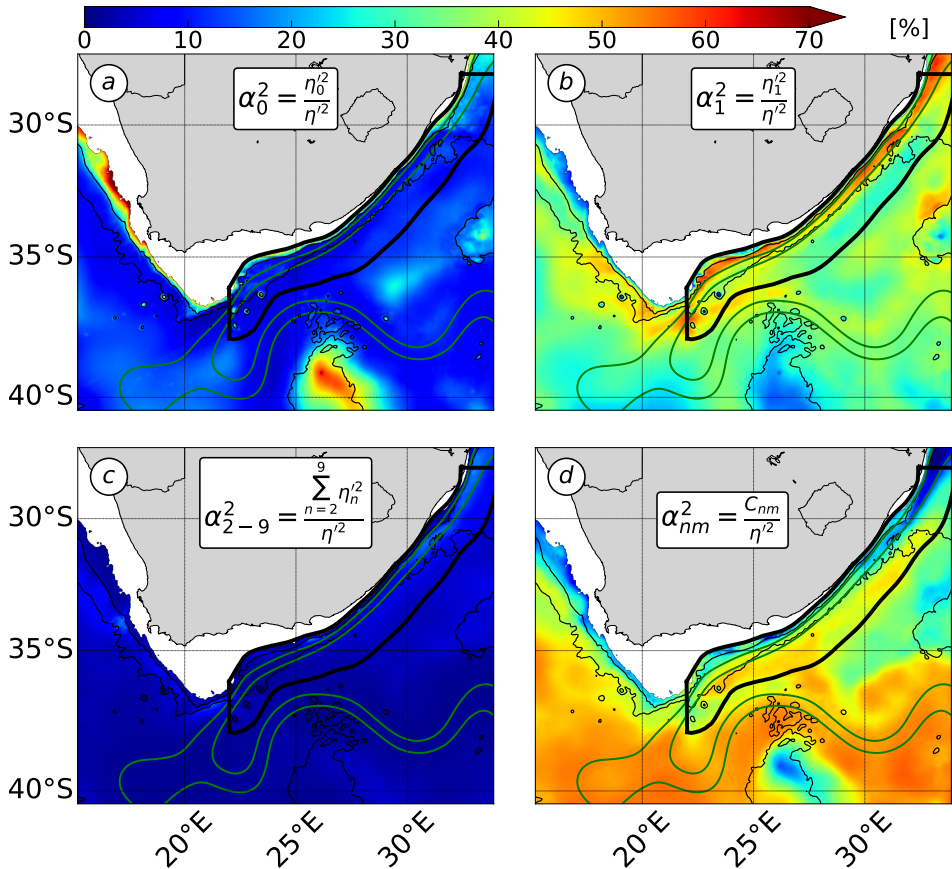


Figure B1: Partitioning of  $\eta$  variance ( $\alpha_n^2$ ) between the vertical modes categories : (a)  $n = 0$ , (b)  $n = 1$ , (c)  $n = 2 - 9$  and (d) the intermodal coupling term  $C_{nm}$  [%] (Eq. B1). (cf. Figure 1 for a detailed caption). The  $\eta$  variance largely partitions into (b) the 1<sup>st</sup> baroclinic mode and more weakly into (a) the barotropic mode, which both contribute to  $EPW_{(i,iii)}$  (Eq. 11; Figure 2c).

$\eta'^2$  mainly partitions into the individual 1<sup>st</sup> baroclinic mode ( $38 \pm 2\%$  in the WB region) and the intermodal coupling term ( $36 \pm 2\%$  in the WB region). It also partitions more weakly, but still significantly into the individual barotropic mode ( $16 \pm 4\%$  in the WB region) (Figure B1). The partitioning of  $\eta'^2$  is partially consistent with the usual interpretation of  $\eta$  primarily reflecting the 1<sup>st</sup> baroclinic mode (Wunsch, 1997; Smith & Vallis, 2001). However, it indicates that the vertical structure of mesoscale eddies – formally represented by the combination of the barotropic ( $n = 0$ ) and 1<sup>st</sup> baroclinic modes ( $n = 1$ ) (Wunsch, 2007; Smith & Vallis, 2001; Venaille et al., 2011; Tedesco et al., 2022) – can be accurately inferred from  $\eta$  field.

703 **Appendix C Contribution of ageostrophic motions to the true EPW by**  
 704 **the Rhines scale**

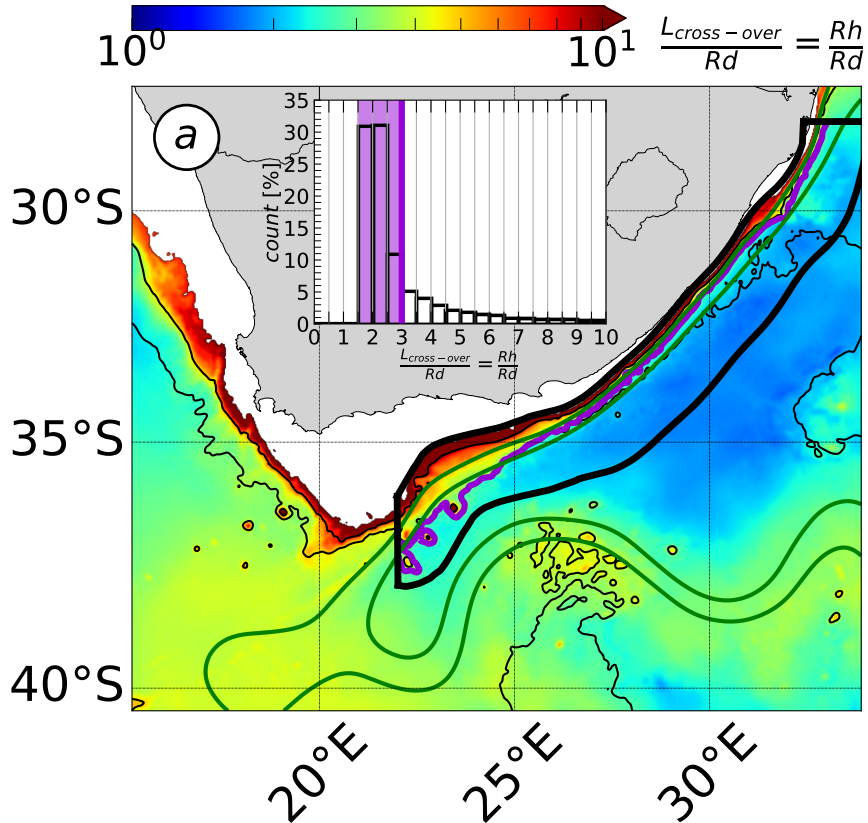


Figure C1: (a) Ratio  $\frac{L_{\text{cross-over}}}{Rd} = \frac{Rh}{Rd}$  ( $Rh = \frac{1}{H} \int_{-H}^{\eta} \left( \sqrt{\frac{\|\mathbf{u}'\|}{\beta}} \right) dz$ , with  $\|\mathbf{u}'\|$  the magnitude of mesoscale eddies velocity). The purple line denotes  $\frac{Rh}{Rd}$  70 % percentile, the green contours denote the 0.25 m and 0.5 m isolines of time-averaged  $\eta$  and black contours denote the 1000 m and 3000 m isobaths. The terms count in the WB region [%] is shown as barplot, where purple shaded areas denote the 70 % percentile range of values. (a)  $\frac{Rh}{Rd} \gg 1$  in the WB region, resulting in  $L_{\text{eddy}} (\geq Rd)$  to fall in the range of dominating partially ageostrophic EPW, compared to the  $\beta$ -effect.

705 The Rhines scale ( $Rh$ ) is defined in turbulence geostrophic theory to mark the transition  
 706 from an advectively-dominated ( $Rh \ll L$ ) to a Rossby waves-dominated ( $Rh \gg L$ )  
 707 turbulent regime (Rhines, 1975).  $Rh$  is also emphasized by our scale analysis to mark the  
 708 transition from a partially ageostrophic-dominated to a  $\beta$ -effect-dominated EPW (section  
 709 4.4).

710

711 We infer  $Rh$  for the mesoscale eddies simulated by the  $\text{dx} \sim 2.5$  km numerical grid, as  
 712 follows :  $Rh = \frac{1}{H} \int_{-H}^{\eta} \left( \sqrt{\frac{\|\mathbf{u}'\|}{\beta}} \right) dz$  with  $\|\mathbf{u}'\|$  the magnitude of mesoscale eddies velocity.  
 713  $\frac{Rh}{Rd} \sim O(1.5 - 3)Rd$  in 70 % of the WB region, with larger ratio located at the inner front of  
 714 the Agulhas Current (Figure C1). It results in  $L_{eddy}$  ( $L_{eddy} \geq Rd$ ) to fall in the WB region  
 715 in the range of an advectively-dominated turbulent.

716

717 Along with  $L_{cross-over} = \frac{\zeta'_{RMS}}{\beta}$  (Eq. 13; Figure 3b),  $Rh$  confirms that the partially  
 718 ageostrophic EPW dominates the  $\beta$ -effect. It questions the use of satellite altimetry data to  
 719 infer EPW (Eq. 4). However, the impact of the geostrophic approximation (i) on AEKE  
 720 must be assessed to conclude on the use of satellite altimetry data to infer the EKE flux  
 721 divergence.

**722 Acknowledgments**

723 This work was granted access to the HPC resources of IDRIS under the allocation A0040107630  
724 made by GENCI at Paris, France, and of the HPC facilities DATARMOR of “Pôle de Calcul  
725 Intensif pour la Mer” at Ifremer, Brest, France. This work was supported by the Ifremer  
726 and the Brittany region for PhD funding. We also gratefully acknowledge support from  
727 the French National Agency for Research (ANR) through the projects DEEPER (ANR-19-  
728 CE01-0002-01) and the project DIEGO of the CNES/TOSCA SWOT program. WOES36  
729 model outputs are available online at [http://dap.saeon.ac.za/thredds/catalog/SAEON](http://dap.saeon.ac.za/thredds/catalog/SAEON.EGAGASINI.10000)  
730 .EGAGASINI/2019.Penven/DAILY\_MEANS/1\_36\_degree/catalog.html (DOI: 10.15493/SAEON.EGAGASINI.10000)  
731 The AVISO data are available at [www.aviso.altimetry.fr](http://www.aviso.altimetry.fr), the WOA18 and WOCE cli-  
732 matologies are available at [www.nodc.noaa.gov/OC5/woa18/](http://www.nodc.noaa.gov/OC5/woa18/) and <https://icdc.cen.uni-hamburg.de/thredds/catalog/ftpthredds/woce/catalog.htm>.

734 **References**

- 735 Adcock, S., & Marshall, D. (2000). Interactions between geostrophic eddies and the mean  
736 circulation over large-scale bottom topography. *Journal of physical oceanography*, 30(12),  
737 3223–3238.
- 738 Capó, E., Orfila, A., Mason, E., & Ruiz, S. (2019). Energy conversion routes in the western  
739 mediterranean sea estimated from eddy–mean flow interactions. *Journal of Physical  
740 Oceanography*, 49(1), 247–267.
- 741 Charney, J. G. (1971). Geostrophic turbulence. *Journal of the Atmospheric Sciences*, 28(6),  
742 1087–1095.
- 743 Chelton, D., Deszoeke, R., Schlax, M., El Naggar, K., & Siwertz, N. (1998). Geographical  
744 variability of the first baroclinic Rossby radius of deformation. *Journal of Physical  
745 Oceanography*, 28(3), 433–460.
- 746 Chelton, D., Schlax, M., & Samelson, R. (2011). Global observations of nonlinear mesoscale  
747 eddies. *Progress in oceanography*, 91(2), 167–216.
- 748 Chelton, D., Schlax, M., Samelson, R., & de Szoeke, R. (2007). Global observations of large  
749 oceanic eddies. *Geophysical Research Letters*, 34(15).
- 750 Chen, R., Flierl, G., & Wunsch, C. (2014). A description of local and nonlocal eddy–  
751 mean flow interaction in a global eddy-permitting state estimate. *Journal of Physical  
752 Oceanography*, 44(9), 2336–2352.
- 753 Cushman-Roisin, B., & Beckers, J.-M. (2011). *Introduction to geophysical fluid dynamics:  
754 physical and numerical aspects*. Academic press.
- 755 Debreu, L., Marchesiello, P., Penven, P., & Chambon, G. (2012). Two-way nesting in split-  
756 explicit ocean models: Algorithms, implementation and validation. *Ocean Modelling*,  
757 49–50, 1–21.
- 758 Ducet, N., Traon, P.-Y. L., & Reverdin, G. (2000). Global high-resolution mapping of ocean  
759 circulation from TOPEX/Poseidon and ERS-1 and-2. *Journal of Geophysical Research:  
760 Oceans*, 105(C8), 19477–19498.
- 761 Eliot, S., & Beal, L. M. (2015). Characteristics, Energetics, and Origins of Agulhas  
762 Current Meanders and Their Limited Influence on Ring Shedding. *Journal of Physical  
763 Oceanography*, 45(9), 2294–2314. doi: 10.1175/JPO-D-14-0254.1
- 764 Evans, D., Frajka-Williams, E., & Garabato, A. N. (2022). Dissipation of mesoscale eddies  
765 at a western boundary via a direct energy cascade. *Scientific Reports*, 12(1), 1–13.
- 766 Evans, D., Frajka-Williams, E., Garabato, A. N., Polzin, K., & Forryan, A. (2020).  
767 Mesoscale eddy dissipation by a ‘zoo’ of submesoscale processes at a western boundary.  
768 *Journal of Geophysical Research: Oceans*, e2020JC016246.
- 769 Ferrari, R., & Wunsch, C. (2009). Ocean circulation kinetic energy: Reservoirs, sources,  
770 and sinks. *Annual Review of Fluid Mechanics*, 41.
- 771 Gill, A. (1982). *Atmosphere-ocean dynamics (international geophysics series)*. academic  
772 press.
- 773 Gill, A., Green, J., & Simmons, A. (1974). Energy partition in the large-scale ocean  
774 circulation and the production of mid-ocean eddies. *Deep sea research and oceanographic  
775 abstracts*, 21(7), 499–528.
- 776 Gouretski, V., & Koltermann, K. (2004). WOCE global hydrographic climatology. *Berichte  
777 des BSH*, 35, 1–52.
- 778 Gula, J., Molemaker, M., & McWilliams, J. (2015). Gulf Stream dynamics along the  
779 Southeastern U.S. Seaboard. *J. Phys. Oceanogr.*, 45(3), 690–715.
- 780 Gula, J., Molemaker, M., & McWilliams, J. (2016). Submesoscale dynamics of a Gulf  
781 Stream frontal eddy in the South Atlantic Bight. *Journal of Physical Oceanography*,  
782 46(1), 305–325.
- 783 Halo, I., Penven, P., Backeberg, B., Ansorge, I., Shillington, F., & Roman, R. (2014).  
784 Mesoscale eddy variability in the southern extension of the East Madagascar Current:  
785 Seasonal cycle, energy conversion terms, and eddy mean properties. *Journal of Geophysical  
786 Research: Oceans*, 119(10), 7324–7356.

- Harrison, D. E., & Robinson, A. R. (1978). Energy analysis of open regions of turbulent flows—Mean eddy energetics of a numerical ocean circulation experiment. *Dynamics of Atmospheres and Oceans*, 2(2), 185–211.
- Jamet, Q., Deremble, B., Wienders, N., Uchida, T., & Dewar, W. (2021). On wind-driven energetics of subtropical gyres. *Journal of Advances in Modeling Earth Systems*, 13(4), e2020MS002329.
- Kang, D., & Curchitser, E. (2015). Energetics of eddy-mean flow interactions in the Gulf Stream region. *Journal of Physical Oceanography*, 45(4), 1103–1120.
- Kelly, S. (2016). The vertical mode decomposition of surface and internal tides in the presence of a free surface and arbitrary topography. *Journal of Physical Oceanography*, 46(12), 3777–3788.
- Kelly, S., Nash, J., & Kunze, E. (2010). Internal-tide energy over topography. *Journal of Geophysical Research: Oceans*, 115(C6).
- Kelly, S., Nash, J., Martini, K., Alford, H. M., & Kunze, E. (2012). The cascade of tidal energy from low to high modes on a continental slope. *Journal of physical oceanography*, 42(7), 1217–1232.
- Li, J., Roughan, M., & Kerry, C. (2021). Dynamics of interannual eddy kinetic energy modulations in a western boundary current. *Geophysical Research Letters*, e2021GL094115.
- Locarnini, M., Mishonov, A., Baranova, O., Boyer, T., Zweng, M., Garcia, H., ... others (2018). *World ocean atlas 2018, volume 1: Temperature* [Dataset]. ARCHIMER. Retrieved from [https://data.nodc.noaa.gov/woa/WOA18/DOC/woa18\\_vol1.pdf](https://data.nodc.noaa.gov/woa/WOA18/DOC/woa18_vol1.pdf)
- Lutjeharms, J. (2006). *The Agulhas Current* (Vol. 2). Springer.
- Masuda, A. (1978). Group velocity and energy transport by Rossby waves. *Journal of Oceanography*, 34(1), 1–7.
- Müller, P., McWilliams, J., & Molemaker, M. (2005). *Routes to dissipation in the ocean: The 2D/3D turbulence conundrum*. Cambridge University Press Cambridge.
- Nikurashin, M., & Ferrari, R. (2010). Radiation and dissipation of internal waves generated by geostrophic motions impinging on small-scale topography: Theory. *Journal of Physical Oceanography*, 40(5), 1055–1074.
- Paldor, N., & Lutjeharms, J. (2009). Why is the stability of the Agulhas Current geographically bi-modal? *Geophysical Research Letters*, 36(14), n/a–n/a. Retrieved from <http://dx.doi.org/10.1029/2009GL038445> (L14604) doi: 10.1029/2009GL038445
- Perfect, B., Kumar, N., & Riley, J. (2020). Energetics of Seamount Wakes. Part I: Energy Exchange. *Journal of Physical Oceanography*, 50(5), 1365–1382.
- Qiu, B., Chen, S., Klein, P., Wang, J., Torres, H., Fu, L.-L., & Menemenlis, D. (2018). Seasonality in transition scale from balanced to unbalanced motions in the world ocean. *Journal of Physical Oceanography*, 48(3), 591–605.
- Rhines, P. (1975). Waves and turbulence on a beta-plane. *Journal of Fluid Mechanics*, 69(3), 417–443.
- Scott, R., & Furnival, D. (2012). Assessment of traditional and new eigenfunction bases applied to extrapolation of surface geostrophic current time series to below the surface in an idealized primitive equation simulation. *Journal of physical oceanography*, 42(1), 165–178.
- Shchepetkin, A., & McWilliams, J. (2005). The Regional Oceanic Modeling System (ROMS): A split-explicit, free-surface, topography-following- coordinate ocean model. *Ocean Modelling*, 9, 347–404.
- Smith, K., & Vallis, G. (2001). The scales and equilibration of midocean eddies: Freely evolving flow. *Journal of Physical Oceanography*, 31(2), 554–571.
- Tedesco, P., Gula, J., Ménesguen, C., Penven, P., & Krug, M. (2019). Generation of submesoscale frontal eddies in the Agulhas Current. *Journal of Geophysical Research: Oceans*, 124(11), 7606–7625.
- Tedesco, P., Gula, J., Penven, P., & Ménesguen, C. (2022). Mesoscale Eddy Kinetic Energy budgets and transfers between vertical modes in the Agulhas Current. *Journal of Physical Oceanography*.

- 841 Torres, H., Klein, P., Menemenlis, D., Qiu, B., Su, Z., Wang, J., ... Fu, L.-L. (2018).  
842 Partitioning ocean motions into balanced motions and internal gravity waves: A modeling  
843 study in anticipation of future space missions. *Journal of Geophysical Research: Oceans*,  
844 123(11), 8084–8105.
- 845 Venaille, A., Vallis, G., & Smith, K. (2011). Baroclinic turbulence in the ocean: Analysis  
846 with primitive equation and quasigeostrophic simulations. *Journal of Physical Oceanography*,  
847 41(9), 1605–1623.
- 848 Vic, C., Roullet, G., Carton, X., & Capet, X. (2014). Mesoscale dynamics in the Arabian  
849 Sea and a focus on the Great Whirl life cycle: A numerical investigation using ROMS.  
850 *Journal of Geophysical Research: Oceans*, 119(9), 6422–6443.
- 851 Wunsch, C. (1997). The vertical partition of oceanic horizontal kinetic energy. *Journal of  
852 Physical Oceanography*, 27(8), 1770–1794.
- 853 Wunsch, C. (2007). The past and future ocean circulation from a contemporary perspective.  
854 *Geophysical Monograph-American Geophysical Union*, 173, 53.
- 855 Yan, X., Kang, D., Curchitser, E., & Pang, C. (2019). Energetics of eddy-mean flow  
856 interactions along the western boundary currents in the North Pacific. *Journal of Physical  
857 Oceanography*, 49(3), 789–810.
- 858 Yang, Y., & Liang, X. S. (2016). The instabilities and multiscale energetics underlying  
859 the mean-interannual-eddy interactions in the Kuroshio Extension region. *Journal of  
860 Physical Oceanography*, 46(5), 1477–1494.
- 861 Yang, Z., Zhai, X., Marshall, D., & Wang, G. (2021). An Idealized Model Study of Eddy  
862 Energetics in the Western Boundary “Graveyard”. *Journal of Physical Oceanography*,  
863 51(4), 1265–1282.
- 864 Yankovsky, E., Zanna, L., & Smith, K. (2022). Influences of Mesoscale Ocean Eddies on  
865 Flow Vertical Structure in a Resolution-Based Model Hierarchy. *Earth and Space Science  
866 Open Archive*, 60. Retrieved from <https://doi.org/10.1002/essoar.10511501.1> doi:  
867 10.1002/essoar.10511501.1
- 868 Zhai, X., Johnson, H., & Marshall, D. (2010). Significant sink of ocean-eddy energy near  
869 western boundaries. *Nature Geoscience*, 3(9), 608.
- 870 Zweng, M., Seidov, D., Boyer, T., Locarnini, M., Garcia, H., Mishonov, A., ... others  
871 (2019). *World ocean atlas 2018, volume 2: Salinity* [Dataset]. ARCHIMER. Retrieved  
872 from [https://data.nodc.noaa.gov/woa/WOA18/DOC/woa18\\_vol2.pdf](https://data.nodc.noaa.gov/woa/WOA18/DOC/woa18_vol2.pdf)